Alma Mater Studiorum – Università di Bologna

Dottorato di Ricerca in Ingegneria Elettronica, Telecomunicazioni e Tecnologie dell'Informazione

33° Ciclo

Settore Concorsuale: 09/F1

Settore Scientifico Disciplinare: ING-INF/02

CAMPI ELETTROMAGNETICI

MICROWAVE RADAR AND WIRELESS POWER TRANSFER SYSTEMS FOR BIOMEDICAL AND INDUSTRIAL APPLICATIONS

Presentata da:
Giacomo Paolini

Supervisore:
Prof. Alessandra Costanzo

Coordinatore Dottorato:
Prof. Alessandra Costanzo

Co-Supervisore:
Prof. Diego Masotti

Esame Finale Anno 2021

<u>Index</u>

3. A 5.8 GHz Self-Injection Locked Oscillator for Breath Detection

4. A WPT-IoT System for Predictive Maintenance in Electromagnetically Harsh Industrial Environments

5. Conclusion

References

Abstract

Over the last years, modern technologies such as radiofrequency identification (RFID), wireless sensor networks (WSN), and wireless power transfer (WPT) are increasingly gaining attraction, both for the biomedical and the industrial fields of study, intending to achieve the paradigm of the internet of things (IoT). Within this research, different systems have been designed and realized by exploiting these typical IoT applications.

For what concerns the biomedical sphere of interest, it is proving to be more and more urgent to continuously monitor the behaviors and the vital parameters of elderly people to detect as soon as possible any sort of disease or problem. Therefore, a customized 2.45 GHz RFID localization system has been realized in order to simultaneously perform 3-D tracking of multiple tagged people, static or dynamic, in indoor environments, i.e., the retirement homes. Moreover, a 5.8 GHz wearable device for human breath detection has been conceived, making use of the self-injection locked (SIL) radar technique.

Finally, focusing on predictive maintenance, which is increasingly playing a crucial role for industrial, and in particular automotive, applications, it has been presented the design and the validation of a WPT system seamlessly integrated with a WSN platform for remote monitoring

of important parts of the engine, placed in a typical electromagnetically harsh, metal-rich environment, e.g., the engine compartment of a car. Energy is provided wirelessly by means of an RF power source at 2.45 GHz to the low-power wireless sensor nodes located in difficult-to-be-reached positions, allowing to eliminate their periodic battery replacement.

List of Abbreviations

Abbreviation	Explanation
ABS	Acrylonitrile Butadiene Styrene
AI	Artificial Intelligence
AZ	Azimuth
BLE	Bluetooth Low Energy
BT	Bandwidth-Period Product
BW	Bandwidth
CP	Circularly Polarized
CW	Continuous Wave
DC	Direct Current
EH	Energy Harvesting
EIRP	Effective Isotropic Radiated Power
EL	Elevation
EM	Electromagnetic
FCC	Federal Communications Commission
FM	Frequency-Modulated
GFSK	Gaussian Frequency Shift Keying
GPS	Global Positioning System
HB	Harmonic Balance
HPBW	Half-Power Beamwidth
IC	Integrated Circuit
ICNIRP	International Commission on Non-Ionizing Radiation Protection

IIoT	Industrial Internet of Things
IMU	Inertial Measurement Unit
I/O	Input/Output
IoT	Internet of Things
IPS	Indoor Positioning System
ISM	Industrial, Scientific and Medical
LNA	Low-Noise Amplifier
LO	Local Oscillator
LoRa	Long Range
LOS	Line-of-Sight
MCU	Microcontroller Unit
MISO	Master Input Slave Output
MOSI	Master Output Slave Input
MPPT	Maximum Power Point Tracker
MPR	Maximum Power Ratio
NLOS	Non-Line-of-Sight
PCE	Power Conversion Efficiency
PHEMT	Pseudomorphic High Electron Mobility Transistor
PMOS	P-type Metal Oxide Semiconductor
PMU	Power Management Unit
PS	Phase Shifter
PU	Polyurethane
R&D	Research and Development

RF	Radiofrequency
RFID	Radiofrequency Identification
RSSI	Received Signal Strength Indicator
RTC	Real-Time Clock
RToF	Roundtrip Time-of-Flight
SAR	Specific Absorption Rate
SCLK	Serial Clock
SIL	Self-Injection Locked
SILO	Self-Injection Locked Oscillator
SMT	Surface Mount Technology
SoC	System-on-a-Chip
SPI	Serial Peripheral Interface
SPS	Samples Per Second
SS	Slave Select
SWIPT	Simultaneous Wireless Information and Power Transfer
TI	Texas Instruments
UVLO	Undervoltage-Lockout
UWB	Ultra-Wideband
VCO	Voltage-Controlled Oscillator
VNA	Vector Network Analyzer
WBAN	Wireless Body Area Network
WPT	Wireless Power Transfer
WSN	Wireless Sensor Network

Introduction

This chapter is based on the following publications:

G. Paolini, D. Masotti, F. Antoniazzi, T. Salmon Cinotti, and A. Costanzo, "Fall Detection and 3-D Indoor Localization by a Custom RFID Reader Embedded in a Smart e-Health Platform," IEEE Transactions on Microwave Theory and Techniques, vol. 67, no. 12, pp. 5329-5339, Dec. 2019. © 2019 IEEE

F. Antoniazzi, G. Paolini, L. Roffia, D. Masotti, A. Costanzo, and T. Salmon Cinotti, "A Web of Things Approach for Indoor Position Monitoring of Elderly and Impaired People," 21st Conference of Open Innovations Association (FRUCT), Helsinki, Finland, pp. 51-56, 2017. © 2017 IEEE

G. Paolini, M. Feliciani, D. Masotti, and A. Costanzo, "Experimental Study of a Self-Oscillating Antenna at 5.8 GHz for Breath Monitoring," IEEE-APS Topical Conference on Antennas and Propagation in Wireless Communications (APWC), Granada, Spain, pp. 198-200, 2019. © 2019 IEEE

G. Paolini, M. Shanawani, A. Costanzo, F. Benassi, and D. Masotti, "RF Energy On-Demand for Automotive Applications," IEEE MTT-S International Microwave Symposium (IMS), Los Angeles, CA, USA, pp. 1191-1194, 2020. © 2020 IEEE

G. Paolini, M. Guermandi, D. Masotti, M. Shanawani, F. Benassi, L. Benini, and A. Costanzo, "RF-Powered Low-Energy Sensor Nodes for Predictive Maintenance in Electromagnetically Harsh Industrial Environments," Sensors, vol. 21, no. 2, pp. 386-403, Jan. 2021.

1.1. Microwave Radar Systems for Biomedical Applications

Over the last few years, the average age of the world population is meaningfully increasing and, as a consequence, also the number of older people is growing. Therefore, it is proving to be more and more urgent to

continuously monitor the behaviors and consuetudes of the elderly to detect as soon as possible any sort of age-related diseases or problematics, such as Alzheimer's disease or other forms of dementia, that gradually invalidate individuals' physical and mental capabilities.

For instance, Alzheimer's disease is a kind of illness that gradually invalidates many essential human capabilities such as memory, reasoning, conceiving, and learning [1]. Up to now, it is affecting around thirty million people all around the world, estimating that in 2050 one out of eighty-five people will suffer from it. Many research studies have demonstrated that the early signs of Alzheimer's disease that are invisible to family members or even during routine medical examinations, can be diagnosed by observing the movements and the behavior of the patients; for instance, going in the same environment more often than usual, or executing brief repetitive movements in around in a single room or between two rooms, could be seen as an early sign of this disease, whose one of the main characteristics is the space confusion, a sort of space-time disorientation.

Thanks to the wide availability of low-cost, low-power wireless sensor networks (WSN), there has been an always increasing tendency in augmenting living spaces with distributed intelligence, in order to create smart spaces and enabling the internet of things (IoT) paradigm operations. In such scenarios, the radiofrequency identification (RFID)

technology plays an essential role, since remote identification and/or detection of distributed objects is a key issue and a tough task in a wide number of application fields, including smart homes, agriculture, transportation, health and fitness, entertainment, and structural health monitoring.

Hence, a non-invasive continuous identification with the aim of locating patients at hospitals or rest homes can be practical to assist them in real-time: as an example, this could prevent their entrance into an unsafe zone, control if they fall to the ground or if they are lying in the bed for a long time and they need to go for a walk or to take drugs at specified times [2].

A. Smart IoT Solutions for Independent Elderly

In literature [3], [4], some studies investigating the early signs of Alzheimer's disease are already available. Invisible to the family members or even during medical tests, these signs can be recognized by observing the movements of the elderly (i.e., visiting frequently the same rooms, such as the kitchen). Another characteristic of this kind of senile dementia is space confusion, which is also possible to predict because it is often associated with fast repetitive movements in round trips that the patient carries out in the same room. In this way, a relative or the medical

doctor could also easily identify these repetitions, and a diagnosis for the problem can be raised well in advance [5].

In that sense, many pieces of research focused on wireless and RFID technologies enabling smart health care systems [6], movement detection of human body segments [7], people identification [8], localization and activity recognition in smart homes [9], [10], also by means of pan-tilt-zoom cameras [11] and accelerometer [12] for accurate tracking.

In recent years, many systems have been developed to locate the patients affected by this kind of dementia, the majority of them based on global positioning system (GPS) localization systems [13]: this is about lifesaving location devices detecting the position of the tagged person for a certain period at any given time (e.g., every 10 minutes), to monitor the location of the elderly in case of leaving from their own houses or from the retirement homes where they are hosted.

One of these GPS systems includes the localization device in the sole of the shoes [14] and allows the tracking of the loved ones every 10 or 30 minutes; these shoes need to be charged every 48 hours and can be fully charged within two hours.

All these applications can be certainly useful for noticing if a person under surveillance with space confusion troubles has left the building where he lives and is wandering, but they don't give a real answer to the problems that could occur in everyday life: indeed, a non-invasive

continuous system, such as an indoor positioning system (IPS) to locate patients at hospitals or rest homes is certainly essential to assist them in real-time.

IPS is one of the developing new technologies of these last years, and the methods used for its actuation are several and different: among them, it's notable the use of ultra-wideband (UWB) signals [15], that seems to be well promising because the exploitation of a very large range of frequencies allows to avoid the possible effects of fading and shadowing that could occur in all probability in indoor environments at certain frequencies; at the same time, these procedures need a high number of anchors (or readers) inside the room under evaluation and considerable time for the analysis of the incoming data.

In chapter 2, an anchorless solution for tridimensional IPS and remote fall detection is presented. It consists of a portable RFID reader based on a combined design of antennas system, RF front-ends, and digital circuitry, performing simultaneously 3-D tracking of multiple tagged entities, either static or dynamic. A continuous bidimensional electronic beam steering is enabled on the RFID reader in order to implement the monopulse radar technique and to find the angular positions of the RFID tags, both in the azimuth and in the elevation planes; the tags-reader distance estimation is based on received signal strength indicator (RSSI) measurements. In this way, indoor real-time 3-D tracking is made

available for monitoring not only people's movements and occupancy but also accidental falls.

This prototype has been embedded in a smart e-Health platform, called HABITAT (Home Assistance Based on the Internet of Things for the AuTonomy of everybody) [16], which is outlined in Fig. 1.
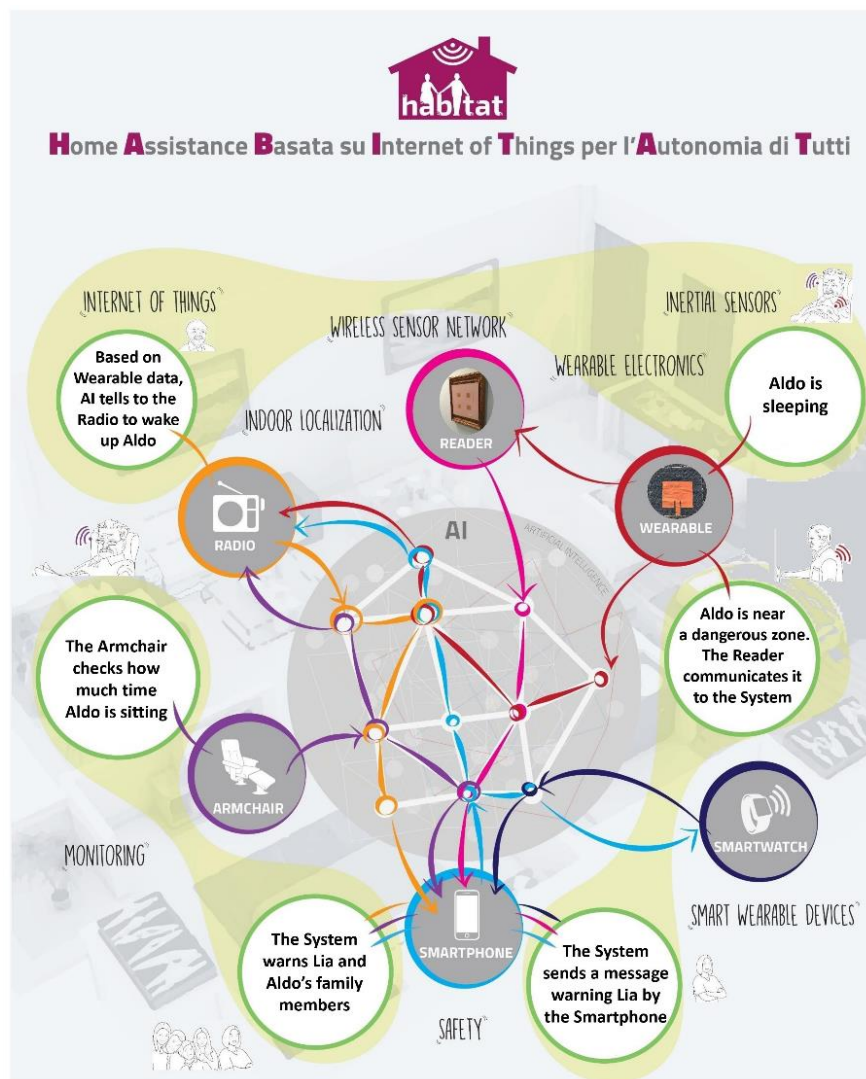

Fig. 1. An envisioned scenario for the HABITAT e-Health platform, the system where the tridimensional RFID indoor localization system has been embedded. [17] © 2019 IEEE

This system consists of several smart objects developed to monitor elderly people living in their own houses or in retirement homes. These objects are interoperable through a unique platform adopting real-time artificial intelligence (AI) procedures to enable decisions and data fusion [18].

The proposed customized RFID localizator interacts in real-time with the e-Health platform to localize tagged people in their daily life environments, prevent their entrance in red zones considered unsafe, control their position, and remotely detect their potential falls.

Starting from the 1-D concept presented in [19], this research details the design, the multi-layer implementation, and the experimental characterization of the front-end and the antenna systems. An extensive measurement campaign is presented for different indoor environments, and the system capabilities for sensing accidental falls are discussed and experimentally demonstrated.

Single and multiple occupancies have also been tested for assessing the localization accuracy in the event of the presence of more than one person.

B. Wearable Sensors for Human Vital Signs Detection

Since the 1970s, wireless technologies have been one of the major subjects of several pieces of research and found great use also in the

healthcare field; this approach consists in the creation of a wireless body area network (WBAN), a network of sensors able to continuously monitor and transmit vital data to healthcare figures, either contactless or directly in contact with the user's body [20]. These short-range devices have been demonstrated to be promising due to their ability to perceive sub-centimeter displacements, as in detecting and monitoring vital activities such as breathing and heartbeat [21]-[25]; indeed, the amplitude of a respiration-induced body movement is considered to range from 0.8 mm to 1.8 mm [21].

Wearable devices have attracted great interest in biomedical applications due to their long-term monitoring capability and the possibility to add wireless connections without a significant increase in terms of energy power consumption; however, robustness, energy consumption, and cost make the challenge of designing these sensors still open.

With the development of semiconductors and integrated circuits (IC), considerable progress has been achieved in hardware miniaturization, thus allowing growth in the production and use of these devices: in particular emerging radar systems present reduced dimensions and weight, low energy consumption, and high sensitivity [22].

Radar devices exploit the Doppler effect to detect the movement of an object. The conventional architecture of a short-range sensor for vital

signals detection foresees an RF signal generated by an oscillator and sent by the transmitting antenna towards the subject, whose chest movements modulate it; the normal breath and heartbeat rate ranges are 0.1 ÷ 0.8 Hz and 0.8 ÷ 3 Hz, respectively [21], and might be accounted for as the modulating signals of the RF carrier received by the wearable system under study. The received signal passes then through a low-noise amplifier (LNA) and interacts with the RF original signal through a mixer from which the baseband signal is finally obtained (Fig. 2).
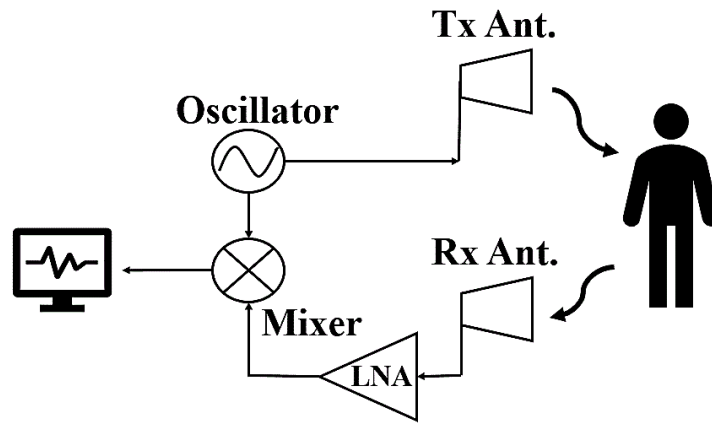
Fig. 2. Conventional architecture of a vital signals detection system. [26] © 2019 IEEE

Chapter 3 describes the realization of a 5.8 GHz self-injection locked (SIL) active antenna to realize a fully wearable, energy-autonomous solution for human breath monitoring [26]. Moreover, a wearable and simple solution for the receiving subsystem has been proposed, exploiting a quarter-wavelength microstrip coupler interacting with the self-injection locked oscillator (SILO) output path and connected to a passive

demodulator/rectifying circuit. In this way, signal processing can be carried out in real-time and on-board. The idea is to support the overall energy requirements of the system, although the full energy-autonomy has not been reached yet.

Finally, in section 3.3, a study on the feasibility of energy harvesting (EH) from modulated signals that are present normally in daily life environments, i.e., Bluetooth low energy (BLE), is presented, reporting the design of the RF-to-DC conversion circuit, considering the input excitation being a signal modulated in frequency. Also, a measurement campaign has been conducted considering as input signal both a frequency-modulated (FM) excitation given by a signal generator and the typical communication packets sent employing a commercial BLE board.

1.2. Wireless Power Transfer Systems for Industrial Applications

In the last decades, the paradigm of the industrial internet of things (IIoT) has become one of the topics that research and development (R&D) areas of enterprises and academia are most interested in.

WSNs brought an always increasing implementation of such technologies to enable seamless connectivity in industrial machinery in general and, for what concerns the advanced automotive sector, several solutions have been tailored to the need of continuous monitoring key-role components with remote sensors to track, almost in real-time rotation, position, speed, temperature, and pressure [27].

One of the main desired characteristics of the wireless sensor nodes is the capability to operate autonomously from EH rather than rely on heavy batteries presenting a limited lifetime, and certainly need a frequent replacement. Several implementations of such sensors have been presented in the literature, e.g., relying on solar [28], kinetic [29], and piezoelectric [30] EH. The main limitation of these solutions is the need to be tailored to the specific deployment; for instance, the node might operate in dark environments or be placed on machinery operating with different levels (and frequency) of vibrations, requiring a careful tuning of the harvester. Having a system capable of operating in a wide number of

scenarios requires to design a complete system integrating both the energy source and the EH-enabled nodes.

For this purpose, the development of wireless power transfer (WPT) solutions and the reduction of the nodes power consumption led to the sensor powering with energy harvesting techniques with the two-fold advantage of conceiving the archetype of "green power", by getting rid of batteries, and of abating the need of maintenance of hardware devices [31]-[37]. In particular, predictive maintenance is increasingly becoming one of the most demanded installments, because of its usefulness for the continuous monitoring of the most critical parts of work equipment and for the prevention of their damage in a timely manner.

Companies have placed great emphasis on these possibilities and are seeking solutions to power their pieces of machinery by means of RF waves, thus significantly reducing the use of cables in industrial plants. For instance, near-field inductive examples have been adopted in that sense [38], [39], as well as prototypes exploiting far-field transmission for industrial applications [40], [41].

Also, several solutions for specific application scenarios exploiting the low-power RFID technology for data communication have been presented, with metal-compatible customized antennas [42], [43].

Studies on the feasibility of sensors powered through RF sources in a car engine are analyzed in [44], where it is clearly stated that the power

transfer efficiency can be extremely variable, not only with respect to the location of the power source and the node but rather to the radio channel in between. It is therefore clear that the integrated design of the sensor nodes and the RF sources (or illuminators) are necessary for a reliable implementation of these systems, considering the complexity of the radio channel.
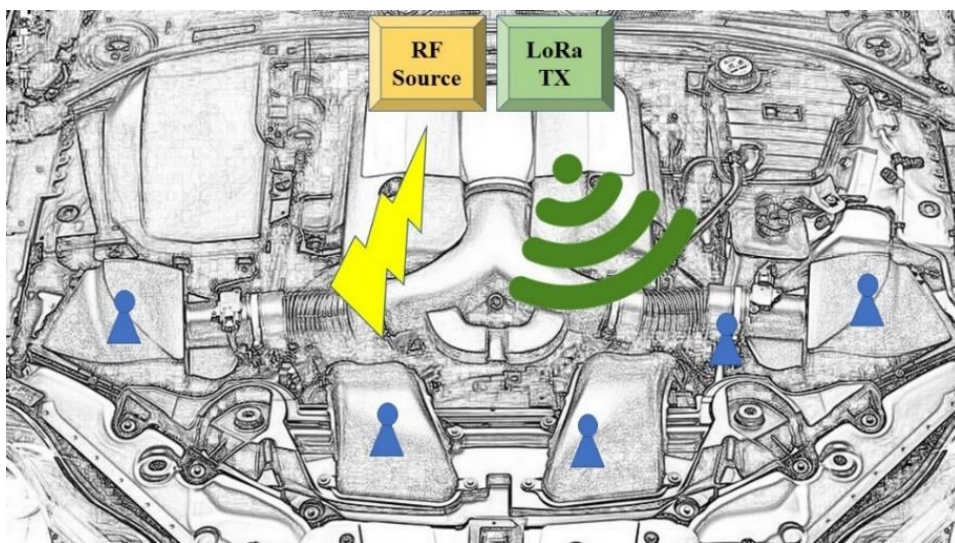

Fig. 3. Illustrative example of the envisioned scenario for a WSN system energized by WPT technology in a harsh automotive environment. The sensor nodes (represented in blue) are scattered around the engine compartment, whereas the power source (yellow) and the communication hub (green) are also shown in one of their possible locations. [45]

Fig. 3 represents a sketch of a fully customized WPT & WSN system for automotive applications that is described in chapter 3, where RF feeding elements (illuminators) at 2.45 GHz are dedicated to energizing the battery-less wireless sensor nodes placed in correspondence with key

points of a car engine, to be continuously monitored in terms of temperature and tridimensional acceleration.

For the illuminator design [46], to comply with the highly complex metallic environment where the system operates, which results in random constructive and/or destructive multi-path electromagnetic (EM) propagations, a 3-D conformal antenna arrangement has been designed for the illuminator, composed of three circularly polarized patch antennas rotated by 45° from each other and incoherently fed by three identical disjointed transmitters.

For the battery-less sensor project, it is worth noticing that the same operating industrial, scientific and medical (ISM) frequency band of 2.4 GHz has been used for both WPT and long range (LoRa) communication, and the integration of the two different antennas has been conceived. A proper selection of the EM spectrum within this band has been chosen to prevent destructive interference of the high WPT signal on the low-power communication signals controlling the isolation of the two node antennas.

Finally, intensive measurement campaigns of the overall system have been presented and discussed both in free space and in the typical working environment where the present work is proposed to be exploited, namely the real engine compartment of a hatchback.

IoT Solutions for Independent Elderly: a Microwave Radar System for Tracking People Occupancy at Home

This chapter is based on the following publications:

G. Paolini, D. Masotti, F. Antoniazzi, T. Salmon Cinotti, and A. Costanzo, "Fall Detection and 3-D Indoor Localization by a Custom RFID Reader Embedded in a Smart e-Health Platform," IEEE Transactions on Microwave Theory and Techniques, vol. 67, no. 12, pp. 5329-5339, Dec. 2019. © 2019 IEEE

G. Paolini, D. Masotti, and A. Costanzo, "Wearable RFID Tag on Denim Substrate for Indoor Localization Applications," 49th European Microwave Conference (EuMC), Paris, France, pp. 504-507, 2019. © 2019 EuMA

2.1. Design of an RFID Reader Enabled Through Monopulse Radar and Electronic Beam Steering Techniques

In this chapter, an alternative system for tridimensional indoor localization is described: in particular, it has the peculiarity to be anchor-free and based on a custom RFID reader system using a beam-steered two-dimensional antenna array composed of four ground-aperture fed patch antennas driven in such a way to perform a fully electronic 2-D beam steering. In this way, in a given room, the reader not only identifies the tags present in the environment but also finds their angular position both in the azimuth and in the elevation planes. By further estimating the distance of the active tags from the reader, through a suitably weighted

evaluation of the tags RSSIs, a short-range 3-D localization is made available. Other techniques reported in the literature are based on roundtrip time-of-flight (RToF) [10], phase delay [47], and group delay [48], but present some kind of drawbacks, e.g., they need several transmitting anchors available in the surrounding space, rely on complex processes of calibration, and sometimes need non-negligible synchronization times between the different anchors.
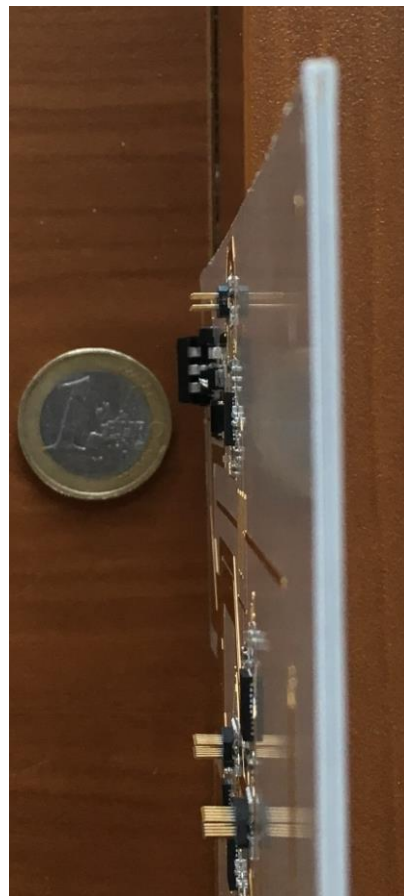

Fig. 4. A typical indoor scenario for people localization and tracking. In this case, two RFID readers are present in the same room and embedded in everyday life objects and furniture (here, a wall lamp). [49] © 2019 IEEE

In Fig. 4, an illustrative example of the targeted scenario is represented. This portable device can be exploited as an agile system for monitoring not only static or moving conditions of people, but also their quantitative elevation, being a possible solution for remote fall detection.

A customized design of a 2.45 GHz RFID reader has been developed to implement bidimensional electronic beam steering [50], taking advantage of the monopulse radar concept [51]. The aim is to enable tridimensional localization of tagged people in EM harsh indoor environments, in the most transparent and non-invasive way. For this purpose, a multi-layer architecture of the RF front-end has been chosen with the radiative elements serving as transmitting and receiving antennas, placed at the opposite side of the RF and digital circuitry.

(a)   (b)

Fig. 5. (a) Stack-up of the entire board of the RFID reader and (b) picture showing the actual board thickness, measuring 6.15 mm also considering the ICs. The only RF substrates, prepreg and copper thickness is about 1.53 mm. [17] © 2019 IEEE

The overall RFID reader board measures 17 x 17 cm^2, and its multi-layered stack-up is shown in Figs. 5: it consists of two external Taconic RF-60A laminates (inner layer #1 and #2; thickness: 0.635 mm, ε_r=6.15); for mechanical stability reasons, the two Taconic layers are held together through a pre-preg FR4 film (thickness: 0.120 mm, ε_r=4.5). The top and bottom copper layers metallization (external foils L1 and L4; thickness: 0.035 mm) host the antenna array and the RF front-end, including the antenna feeding network, and the baseband sub-system.

For this very prototype, the selected working frequency is 2.45 GHz, belonging to the ISM band (2.4 ÷ 2.4835 GHz), to allow the compactness of the overall system, mainly due to the antenna array, and the centimeter-level accuracy of the localization.

A. Antenna Bidimensional Array Design

To implement beam scanning in the azimuth (xy) and the elevation (yz) planes, a two-dimensional array of aperture-coupled patch antennas has been designed, and the picture of the corresponding prototype is shown in Fig. 6: four square patches are fed by means of rectangular apertures obtained in the ground planes (L2 and L3 in Fig. 5 (a)) and excited by proper open feeding lines located in the bottom layer (L4 in Fig. 5 (a)).

Patch array and feeding network correct dimensions have been obtained after optimizations accomplished with the EM simulation software CST Microwave Studio. The quantities to be optimized are: i) the length of the square patches; ii) the patches distances in the xz-plane; iii) the ground aperture dimensions and their relative positions with respect to both the patch in the upper layer (L1) and the feeding line in the bottom layer (L4). The final dimensions adopted for the layout are reported in Table I.
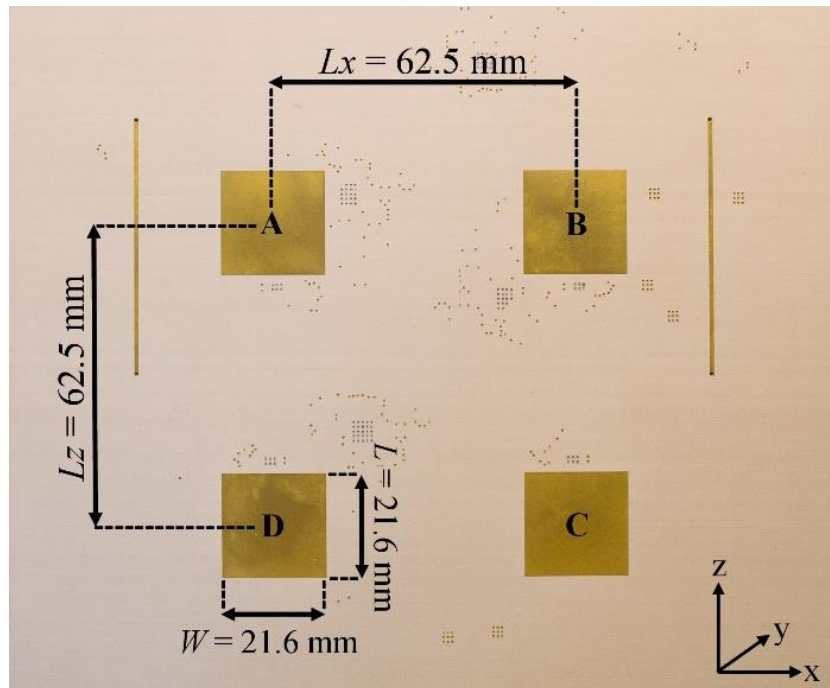

Fig. 6. Photograph of the front layer of the presented RFID reader for 3-D indoor localization, presenting the antenna array. [17] © 2019 IEEE

TABLE I
MAIN COMPONENTS AND LINES DIMENSIONS

Component Description	Dimensions
Overall Reader Board Length	170 mm
Overall Reader Board Width	170 mm
Overall Reader Board Thickness	6.15 mm
Patch Length: L	21.6 mm
Patch Width: W	21.6 mm
Microstrip Width	0.9 mm
Slot Length	1.4 mm
Slot Width	11.80 mm
Slot Distance from Patch Lower Edge	4.66 mm

[17] © 2019 IEEE

The simulated results for the S-parameters of the four-port antenna system are shown in Fig. 7: good matching and low element coupling have been obtained for the present design.
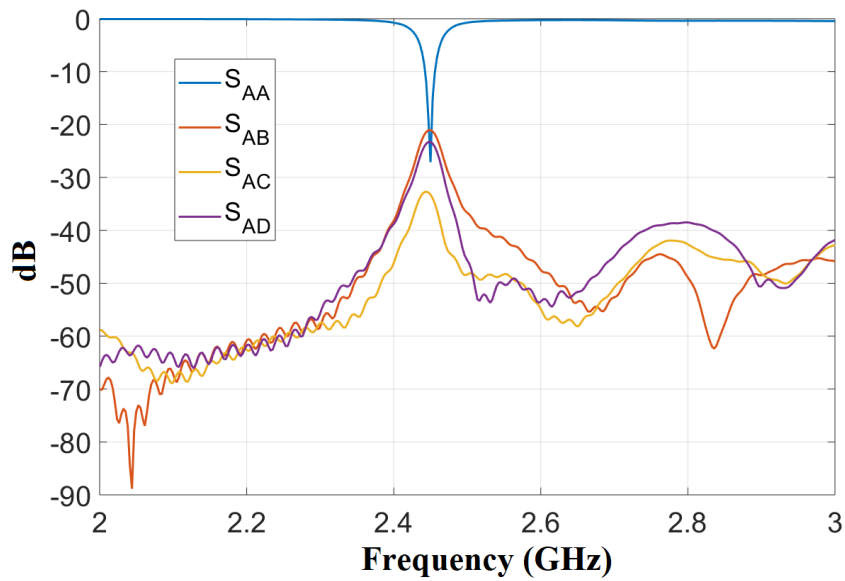
Fig. 7. Scattering parameters of the four-port antenna system (patch antennas and microstrip feeding lines). [17] © 2019 IEEE

B. Master-Slaves Operations of the RF Front-Ends for 2-D Beam Steering Processes

Subsequently, the 2-D monopulse comparator system, or rat race system, has been designed. The schematic layout in microstrip technology is depicted in Fig. 8: the open terminations referred to with the symbols A, B, C, D, are aperture-coupled with the corresponding antennas, while the ports Σ, Δ_{AZ}, Δ_{EL}, and Δ_Q provide the in-phase and the out-of-phase received signals in the azimuth and the elevation planes, plus an auxiliary signal [52], respectively, to be processed by the transceivers connected to them.
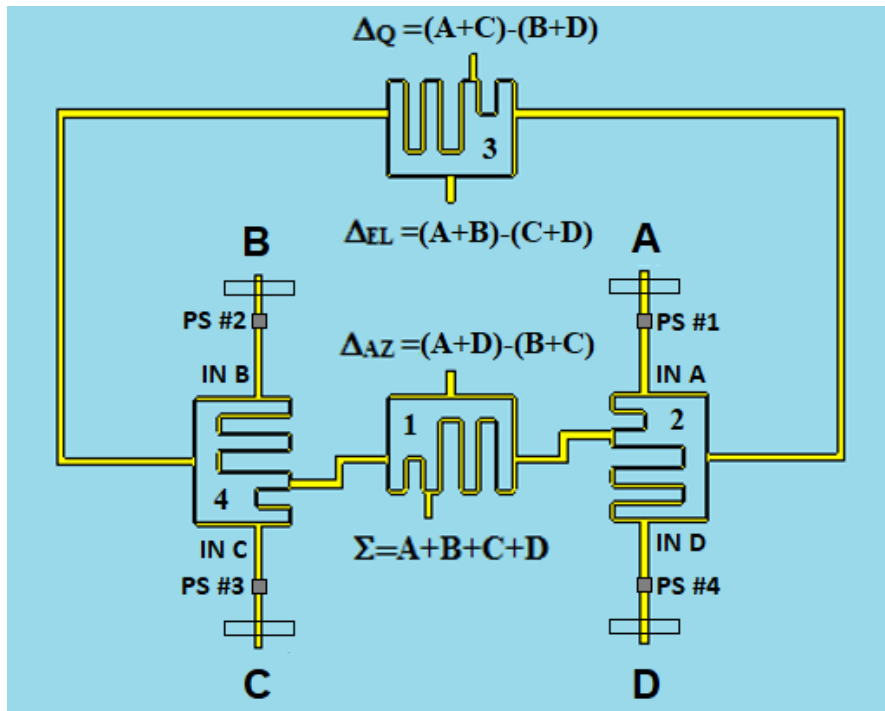
Fig. 8. The RF and digital circuitries lying in the bottom layer: microstrip feeding lines, phase shifters, and monopulse comparator system (or rat race system) are here represented. [17] © 2019 IEEE

For this purpose, and to comply with the overall compactness of the system, four meandered rat-race hybrid couplers [19] (Fig. 8) are suitably connected to each other and, at the same time, to the antenna feeding lines and the RF front-end ports: in this way, the signal combinations superimposed in Fig. 8 are obtained.

In Fig. 9, the back layer of the reader is represented, including the RF and the digital hardware architecture, whereas the principles of operation of the whole system are schematically illustrated in Fig. 10.
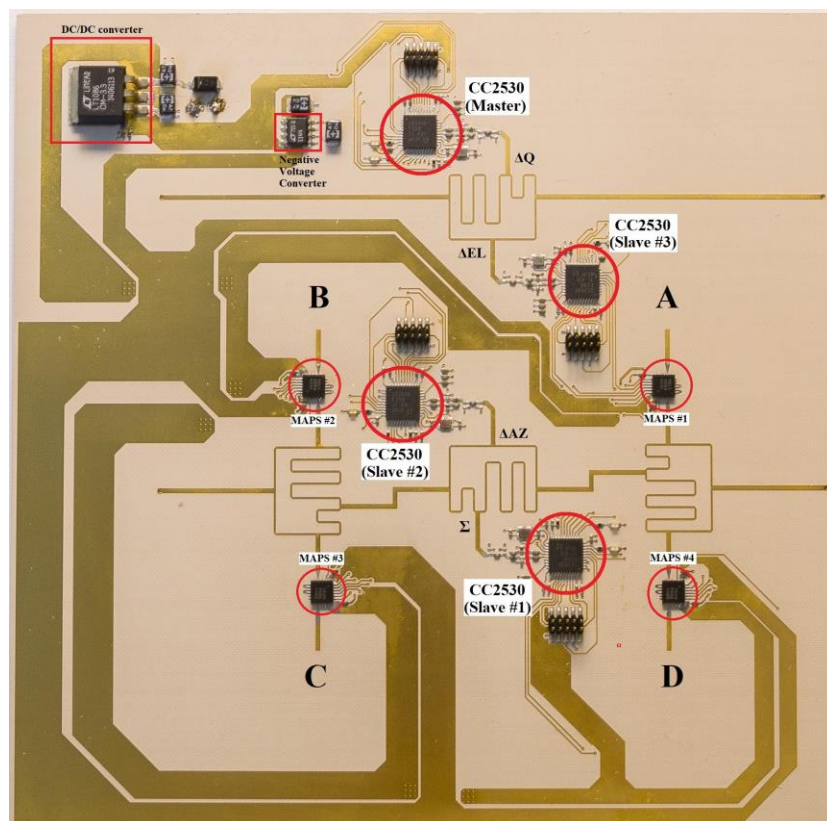
Fig. 9. The back layer of the RFID reader hosting the digital and RF components and the related circuitries. [17] © 2019 IEEE

Four Texas Instruments (TI) CC2530 serial modules have been employed and connected to each of the four abovementioned antenna

system ports: they consist of system-on-a-chip (SoC) configurations integrating the transceiver and the microcontroller unit (MCU), enabling radio communication in the 2.4 GHz band.

Communication among the four MCUs is established and is based on the master-slaves logic: the CC2530 master, connected to the auxiliary port Δ_Q, controls, sends and receives information from the three CC2530 slaves: this is accomplished by the serial peripheral interface (SPI) communication protocol which uses four control signals: i) the serial clock (SCLK) to synchronize the whole communication; ii) a number of slave select (SS) signals (three, for the present case), to activate the proper SoC; iii) master input slave output (MISO); iv) master output slave input (MOSI).
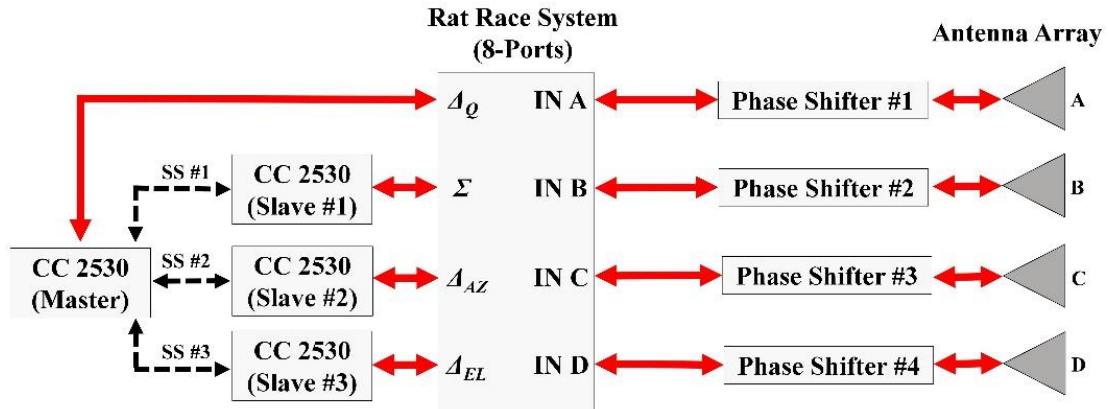

Fig. 10. Block diagram of the hardware architecture and principles of operation (digital input/output and control signals are represented with black dotted lines, whereas the solid red ones represent the RF signals). [17] © 2019 IEEE

To perform the dual-axis (elevation and azimuth) tags localization, a bidimensional electronic beam steering of the Σ and Δ radiation patterns is accomplished.

The beam steering is created by varying the antennas phase excitations through four digital phase shifters (PS), (Macom MAPS-010164) that are inserted along the antenna microstrip feeding lines and controlled by the corresponding MCU (see PS, or MAPS, in Figs. 8 and 9).

The phase selection is based on six-bit binary code so that there are 64 possible phase shifts for each PS: to perform a 360°-coverage of the phase, a step size of 5.6° is used, corresponding to a 1.4°-rotation of the radiation pattern.

Moreover, a DC/DC buck converter (Linear Technology LT1086) and a negative voltage converter (Linear Technology LTC1144) have been introduced in order to guarantee the appropriate supply voltages of 3.3 V and -3.3 V, respectively, to all the ICs.

The concurrent operation of the master and the slaves SoCs allows implementing in real-time the bidimensional beam scanning of the Σ and Δ pattern of the two-dimensional array. To explain the design choices, it is notable to remind that for an array of n identical antennas, aligned along a selected â-direction, with a constant element spacing (L), the complex current phasor at each antenna element port can be expressed as:

$$\Lambda_k e^{(-j\delta_k)} \text{ (A)} \qquad (1)$$

where Λ_k and δ_k are the current amplitude and phase of the array k-th element (with k ranging from 0 to n-1). The array factor, as a function of the elevation and azimuth spherical coordinates, can be cast as follows:

$$F(\theta, \varphi) = \sum_{k=0}^{n-1} \Lambda_k e^{j(\beta k L \hat{a} \cdot \hat{r} - \delta_k)} \qquad (2)$$

where β is the phase propagation constant and $\hat{r}$ is the position unit vector.

If the phase-shift between the currents is constant and equal to δ ($\delta_k = k \cdot \delta$), (2) can be simplified in the following way:

$$F(\theta, \varphi) = \sum_{k=0}^{n-1} [e^{(-j2u)}]^k = e^{[(n-1)u]} \frac{\sin nu}{\sin u} \qquad (3)$$

where $u = (\pi L/\lambda) \cdot \cos \psi - \delta/2$, and $\cos \psi = \hat{a} \cdot \hat{r}$ is a known function of (θ, φ) depending on the alignment direction $\hat{a}$.

The radiation function of the array is then computed from the normalized version of (3), using the radiation function of the array base element $f_0(\theta, \varphi)$:

$$f(\theta, \varphi) = f_0(\theta, \varphi) \left| \frac{F(\theta, \varphi)}{F(\theta_M, \varphi_M)} \right| = f_0(\theta, \varphi) \left| \frac{\sin(n \cdot u)}{n \cdot \sin(u)} \right| \qquad (4)$$

where (θ_M, ϕ_M) represents the maximum radiation direction of both (3) and f_0.

For a linear array of two elements (4) becomes:

$$f(\theta, \varphi) = f_0(\theta, \varphi) |\cos u| \qquad (5)$$

The monopulse radar concept along one direction is realized by an array of two (n=2, in this case) antennas in such a way that if δ=0°, the two antennas are excited in-phase and their radiation function is of the Σ-type (i.e., with a maximum in the broadside direction); on the contrary, if they are excited out-of-phase (δ=180°) their radiation function is of the Δ-type (i.e., with a zero in the broadside direction).

To realize two-dimensional Σ- and Δ-radiation patterns, four patches aligned along the x and z directions to form a two-dimensional array are used as shown in Fig. 6.

The two-dimensional array factor becomes:

$$f(\theta, \varphi) = f_0(\theta, \varphi)|\cos u_x||\cos u_z| \qquad (6)$$

with:

$$u_x = \frac{\pi L_x}{\lambda} \sin \theta \cos \varphi - \frac{\delta_x}{2}$$

$$u_z = \frac{\pi L_z}{\lambda} \cos \theta - \frac{\delta_z}{2} \qquad (7)$$

Moreover, with reference to the array feeding network layout of Fig. 8, it can be observed that the excitations for the antenna elements A, B are out-of-phase with respect to those for elements C, D.

In this way, by means of proper control of the current excitations at the antenna ports, namely the phase coefficients δ_i, with $i = A, B, C, D$, the radiation patterns summarized in Table II are made available.

TABLE II
PHASE SHIFT OF THE ANTENNA FEEDINGS
AND CORRESPONDING PATTERNS

Pattern	δ_A	δ_B	δ_C	δ_D
Σ	0°	0°	180°	180°
Δ_{EL}	0°	0°	0°	0°
Δ_{AZ}	0°	180°	0°	180°
Δ_Q	0°	180°	180°	0°

[17] © 2019 IEEE

Through the phase shifters, placed in between each antenna feeding line (see Figs. 8 and 9), it is possible to electronically vary the absolute phase (δ_i) at each antenna port, in such a way to properly vary the values δ_x and δ_z in (7) between each couple of antennas. In this way, the electronic beam steering is obtained: depending on the selected phase shifts, it is possible to achieve a scanning in both the xy and yz planes.

The electronic beam-steering has been simulated in both planes by means of the post-processing tool of CST Microwave Studio and then measured. Representative results of the Σ and Δ_{EL} patterns in the broadside direction and for 0° and 15° down-rotation are compared in Figs. 11 with those measured in an office scenario. A similar good agreement has been obtained for the azimuth plane patterns.

Approximately, a [-45°, 45°] scan with respect to broadside directions in both the elevation and the azimuth planes has been demonstrated by numerical predictions and measurements.

In this way, the system is able not only to detect a tag in the horizontal plane but also to determine its elevation, due to the accurate scanning capabilities along the vertical plane. In this way, the system can be exploited as a portable "people and/or objects scanner" in 2-D; in particular, it is foreseen to be an interesting device to accurately detect falls of people wearing a tag.
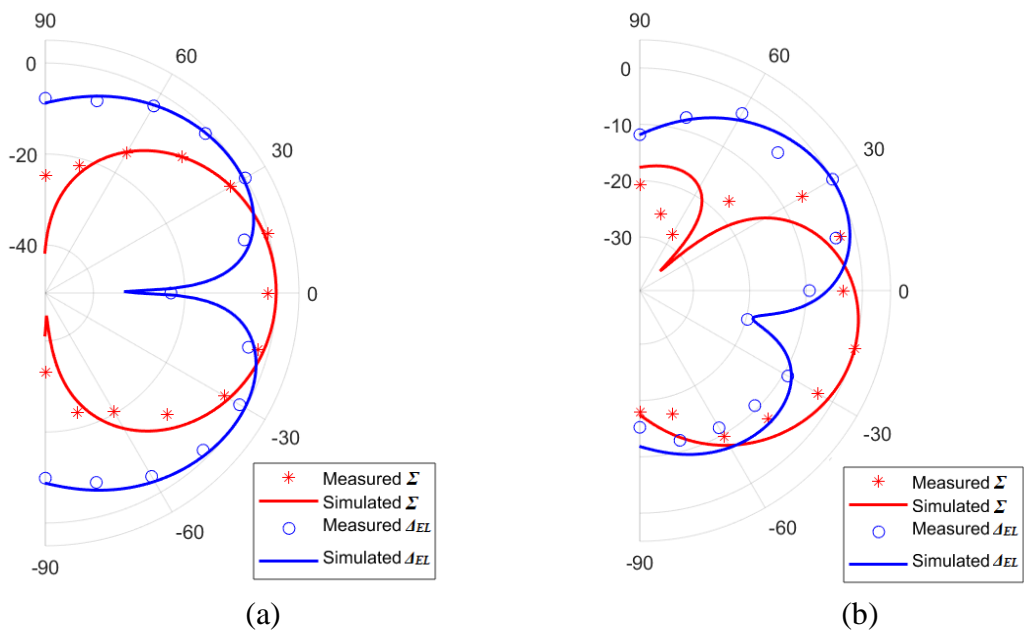

Fig. 11. (a) Normalized monopulse radiation patterns (in dB) of Σ and Δ in the elevation plane in the broadside direction; (b) normalized monopulse-steered radiation patterns (in dB) of Σ and Δ in the elevation plane considering a -15° rotation. [17] © 2019 IEEE

C. Tags Angular Position Detection by Means of the Monopulse Radar Technique

First, the accuracy in localizing the tags' angular positions, both in the azimuth and the elevation planes, has been tested by RSSI measurements at the Σ, Δ_{EL}, and Δ_{AZ} ports, exploiting the system beam steering capabilities.

These experiments have been carried out in a room, whose photograph is shown in Fig. 12, in presence of two tags located as follows: i) at 1- and 3-meters distance from the reader and at the same reader height (125 cm from the ground); ii) 30 cm above and below the reader height.

For these first validation measurements, TI CC2530EM evaluation boards (dimensions: 11.3 x 14.5 cm^2) were used as receiving tags, including the provided monopole antennas (length: 11 cm). The Σ and Δ patterns are stored on-board to compute the tags angular positions by means of the selected figure of merit, i.e., the maximum power ratio (MPR), for the azimuth and the elevation scanning, defined as follows:

$$MPR_{AZ}(dB) = \Sigma\,(dB) - \Delta_{AZ}(dB)$$

$$MPR_{EL}(dB) = \Sigma\,(dB) - \Delta_{EL}(dB)$$

(8)

The MPR_{AZ} and MPR_{EL} are used as the system figures of merit in such a way that detecting the tags' angular position corresponds to the detection of the maximum MPRs.
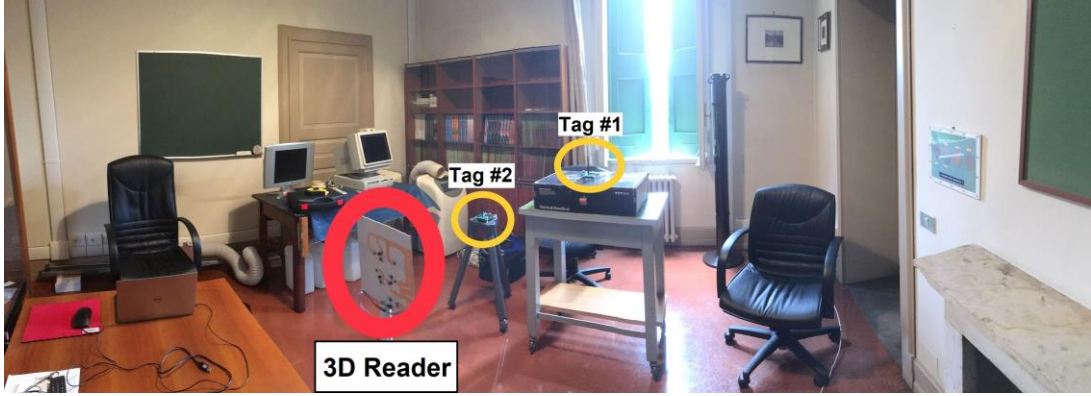
Fig. 12. The indoor scenario where Σ, Δ, MPR retrievals, and the first tridimensional localization measurement took place. [17] © 2019 IEEE

Measurement results are shown in Figs. 13 and 14 and they demonstrate the system's capability to retrieve the corresponding elevation (tags height) and azimuth detection, respectively.
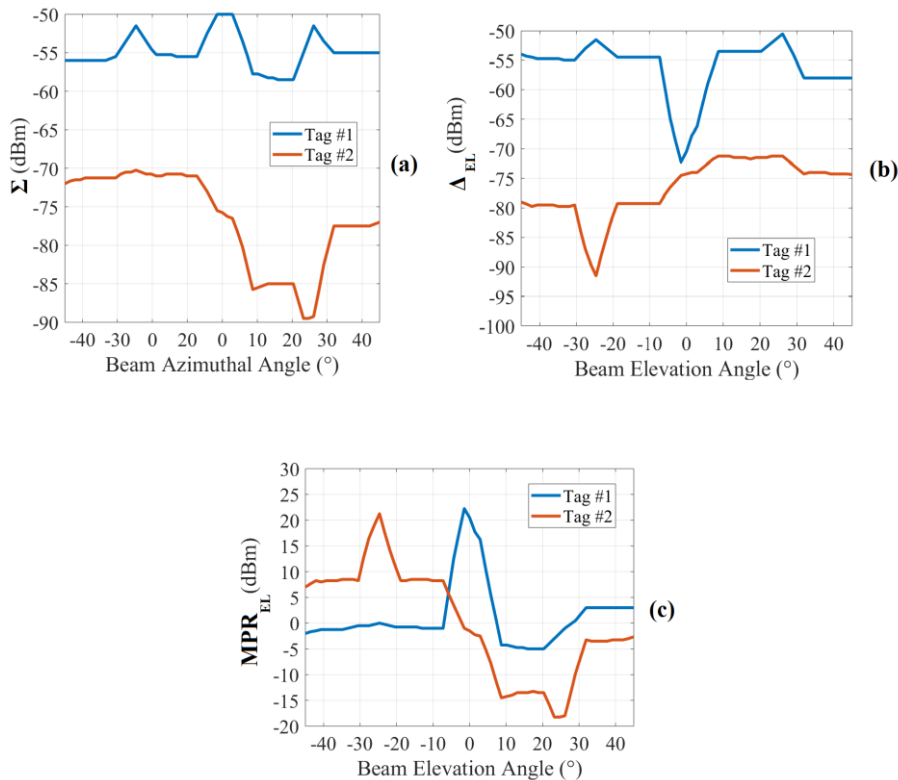

Fig. 13. Elevation detection of two tags: measurements of the RSSI at the (a) Σ port, and at the (b) Δ_{EL} port; (c) resulting MPR. The tags are placed at 1 meter (Tag #1) and 3 meters (Tag #2) of distance from the plane embedding the reader at elevations of 0° and -25°, respectively. [17] © 2019 IEEE
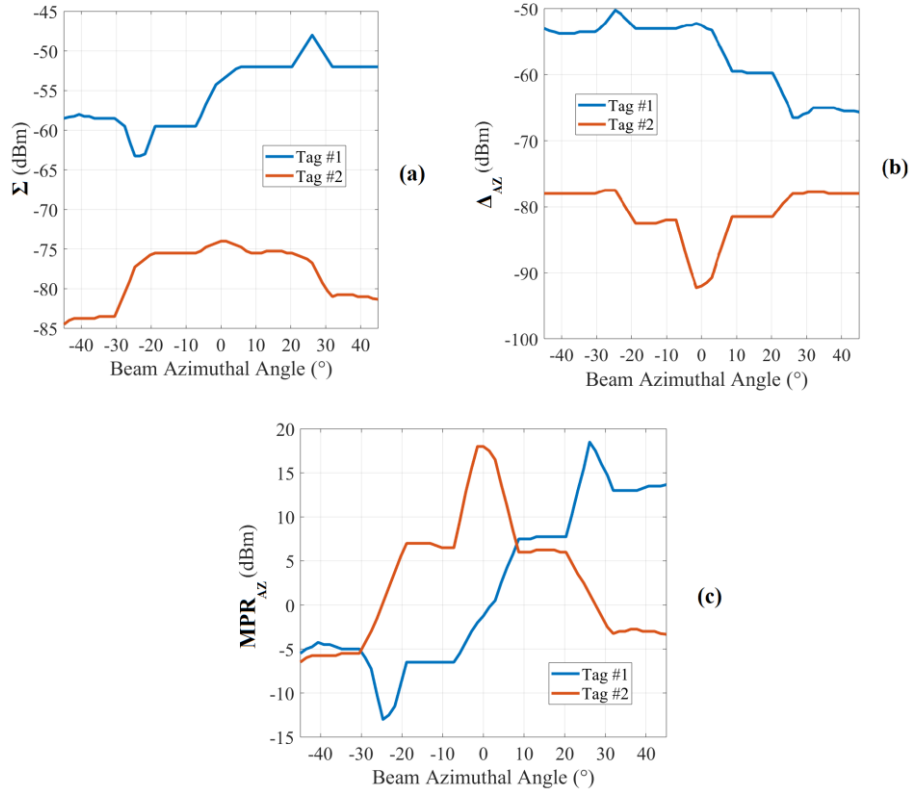
Fig. 14. Azimuth detection of two tags: measurements of the RSSI at the (a) Σ port, and at the (b) Δ_{AZ} port; (c) resulting MPR. The tags are placed at 1 meter (Tag #1) and 3 meters (Tag #2) of distance from the plane embedding the reader at azimuths of +25° and 0°, respectively. [17] © 2019 IEEE

2.2. Tridimensional Localization of Tagged Users in Indoor Environments and Fall Detection Capabilities

In order to provide a full 3-D localization of tagged people, the data collected from the azimuth and elevation beam steering operations are further used to predict the tags-reader distance after carrying out a calibration procedure as follows, once the portable reader is installed in a room: a virtual reference plane is considered at a 1-meter distance from the reader and it is sectorized along with the horizontal and vertical directions in such a way that it is divided into zones. The plane dimensions are chosen based on the reader scanning capabilities. For the present case, a plane of 200-cm width (corresponding to left and right scanning of 67.5°) and 60-cm height (corresponding to an upper and lower scanning of 33.4°) has been considered, divided into a total of nine zones. Tags are subsequently located in the center of each reference zone and the associated received powers P_{0ij} are registered, where i=1, ..., N_{AZ} and j=1, …, N_{EL} (with N_{AZ}=N_{EL}=3) are the numbers of horizontal and vertical chosen segments. Thus, in addition to the azimuth and elevation angular positions, the reader-tag distance d is calculated as follows:

$$d = d_0 \cdot 10^{\frac{(P_{0i,j} - P_{Rm})}{10 \cdot n_{i,j}}} \tag{9}$$

where d_0 is the distance of the reference plane used during calibration, P_{Rm} is the actual instantaneous maximum RSSI (in dBm) received at the Σ-port, and $n_{i,j}$ are the path-loss exponents for the different calibration zones, depending on the radio channel of the environment under consideration (typical values are: $2.7 \div 4.3$ for urban areas, 2 for free space, 1.6 for indoor environments) [53], [54]. For the evaluation of these path-loss exponents in a particular scenario, the above-mentioned calibration measurements of the RSSI values are replicated at a 3-meters distance from the reader, thus deriving the proper $n_{i,j}$ for each calibration zone.

Also in these first 3-D localization measurements, the CC2530EM evaluation board, with its integrated monopole antenna, has been used as a tag. The protocol adopted by these radios for communication is SimpliciTI, the low-power RF network protocol developed by TI; this allows the exchange of information between the reader and the tags regarding their IDs and the corresponding instantaneous RSSI power values. For these measurements, the same path-loss exponent $n_{i,j}=1.9$ resulted to be a suitable choice for all the calibration zones. Some explanatory actual and measured tags positions in the xy plane and the corresponding heights (z-coordinate) are shown in Fig. 15, together with the relative reader location.
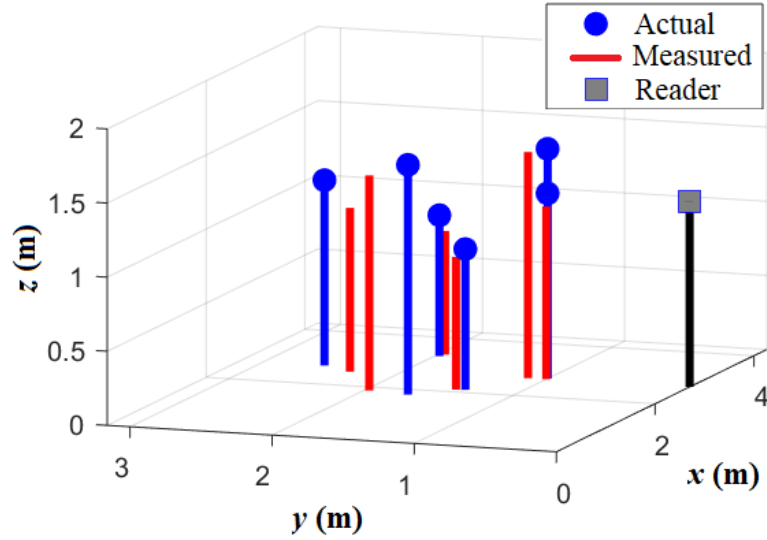
Fig. 15. 3-D localization of six different positions: comparisons between the measured and the actual positions. For these measurements, the evaluation board CC2530EM has been used at the tag side. [49] © 2019 IEEE

In order to obtain a fully wearable RFID tag adequate for indoor localization purposes in everyday environments, the design and realization of prototypes of wearable antennas on flexible textile materials have been conducted. In particular, the antennas have been reproduced on a denim substrate, to be directly designed in jeans clothes, or stitched on other everyday life apparel.

The specific denim material used as a substrate presents a dielectric constant ε_r=1.7, tan(δ)=0.025, and a thickness of 0.78 mm.

The simulation accomplished with the EM software CST Microwave Studio revealed that the increase of the substrate thickness with the employment of two and three overlapping denim layers led to the improvement of the antenna gain. The half-power beamwidth (HPBW) has also been monitored, being one of the most important specifications to

be considered in the project of this type of antennas, that should exhibit a hemispheric radiation pattern as much as possible for effective localization capabilities.
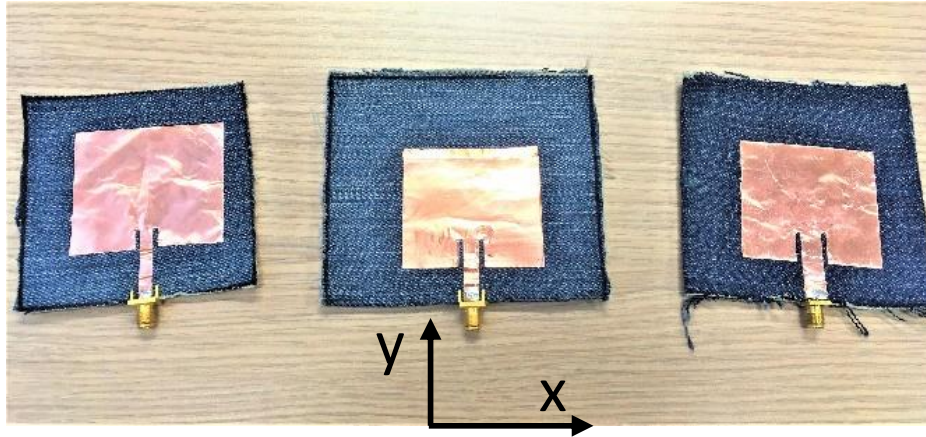

Fig. 16. The three wearable antennas are realized on denim substrate. From left to right, the mono-, bi-, and tri-layer prototypes are represented. [55] © 2019 EuMA

For these reasons, it has been pursued the design and the realization of three different prototypes of this kind of wearable antennas:

- single layer (thickness: 0.78 mm);

- double layer (thickness: 1.56 mm);

- triple layer (thickness: 2.34 mm).

The final length dimensions for the three square patch antennas turned out to be 46.5, 45.8, and 45.7 mm, respectively for the single, double, and triple layer prototypes (Fig. 16).

The microstrip feeding lines have been designed to provide a 50-Ω impedance, analogous to the output impedance of the RF input/output (I/O) matching network of the selected tag transceiver, the TI CC2530

(same of the RFID reader). Although this in-line feeding could not favor size reduction, it can be considered convenient from the ergonomic point of view, because it avoids the presence of a coaxial connector that should be directly in contact with the clothes or even the skin of the user. Moreover, in this case, the continuity of the ground plane is guaranteed avoiding possible effects of detuning or losses of the antenna efficiency that could occur in presence of slots in the ground or the RF feeding circuitry directly in contact with the dispersive tissues of the human body.

First, the resonance frequencies of the antennas have been verified by means of the vector network analyzer (VNA) FieldFox N9923A: in Fig. 17, it is possible to examine the measured reflection coefficient S_{11} magnitude for each of the three prototypes.
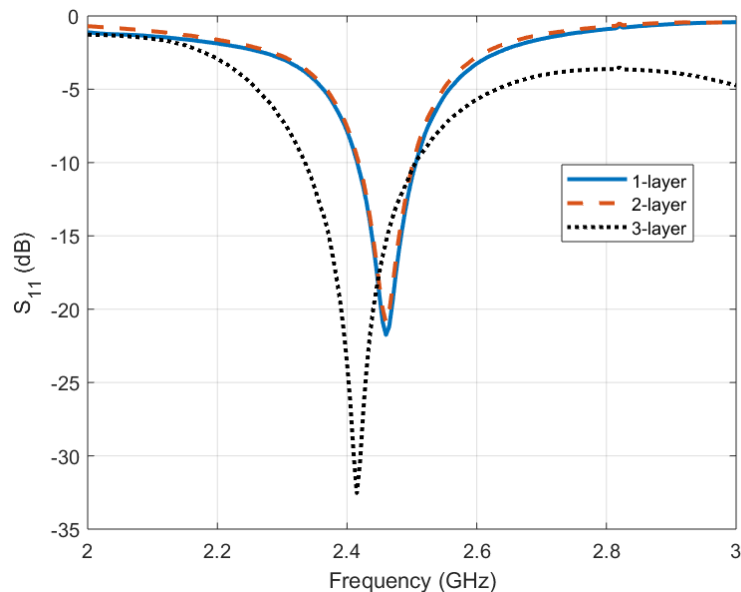

Fig. 17. Measured reflection coefficient magnitude (S_{11}) for the three prototypes realized with denim substrate. [55] © 2019 EuMA

Also, as stated above, two other important characteristics of the antennas to be monitored are certainly the gain and the HPBW. These two parameters have also been quantified experimentally and the results are reported in Table III.

TABLE III
MEASURED ANTENNA GAIN AND HPBW IN FREE SPACE

Antenna	Gain	HPBW
1-layer	3.67 dBi	78°
2-layer	4.17 dBi	81°
3-layer	5.22 dBi	78°

[55] © 2019 EuMA

As foreseen by the EM simulations, too, the thicker the substrate, the higher is the antenna gain. Conversely, the HPBW revealed the same values for the single and three-layer prototypes and a 3-degree extension for the 2-layer model (radiation pattern in Fig. 18).
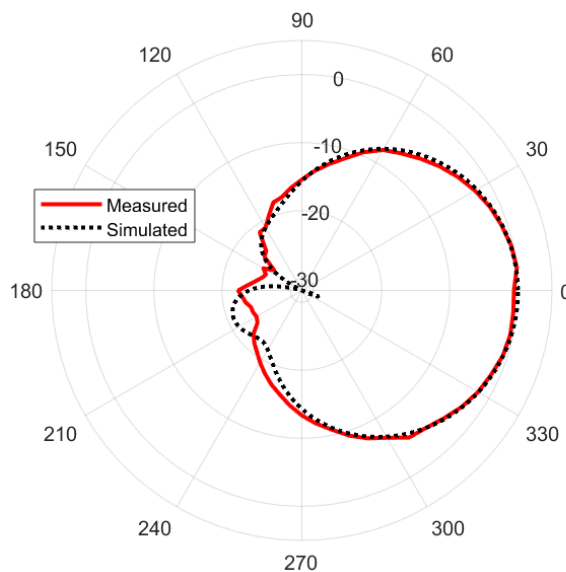
Fig. 18. Normalized measured and simulated polar patterns for the 2-layer denim prototype in free space (horizontal or xz-plane). [55] © 2019 EuMA

A new set of measurements has been conducted with the human body behind the patch antenna simulating tagged people during localization, and the results have not shown significant differences, compared to the free space trials, in terms of antenna gain.

Since antennas realized with wearable (and flexible) materials are designed to be usable stitched on everyday clothes or directly integrated on them, it is necessary to carry out some evaluations regarding their behavior when stressed under a force able to bend them both in the patch H-plane (horizontal or xz-plane, in case of antennas orientation of Fig. 16) and in the E-plane (vertical or yz-plane).

Measurements have not shown any significant variation in terms of gain during the bending tests with the antenna worn on the chest area as an RFID tag for indoor localization should be.
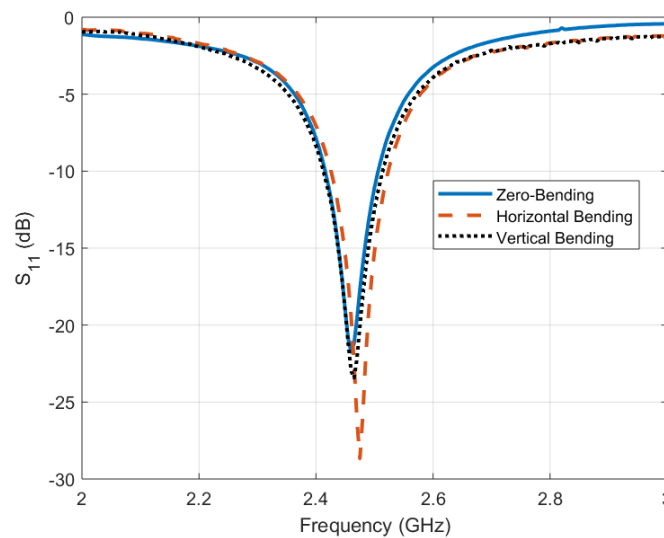

Fig. 19. Measured effects of the horizontal and vertical bending on the reflection coefficient magnitude (S_{11}) of the monolayer prototype compared to the situation without any bending. [55] © 2019 EuMA

51

As shown in Fig. 19 for the single-layer prototype, horizontal and vertical bending moments (with a 90° bending angle) do not introduce any significant frequency detuning effect. Similar behaviors have been recorded for the two multi-layer antennas. It is worth noticing also that, for these measured behaviors, the effect of the crumpled fabric is considered in addition to the effect of horizontal or vertical bending, as it is possible to see from Fig. 16.

For this evaluation, the situations reported in Figs. 20 have been considered: two-sided cylindrical bent conditions with respect to the vertical (Fig. 20 (a)) and horizontal (Fig. 20 (b)) axis with a 90° bending angle.
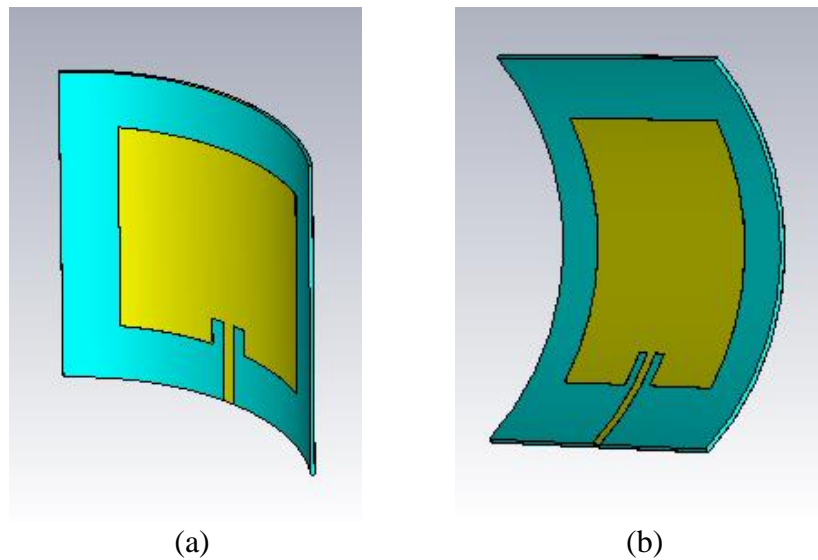

(a)   (b)

Fig. 20. Two-sided (a) vertical and (b) horizontal bending with 90° bending angles considered for the monolayer prototype: these are the situations that have been tested in order to intercept possible detuning effects. [55] © 2019 EuMA

The final dimensions of the denim antenna resulted to be 5 x 5 cm^2, and it has been connected to the TI CC2530 to be worn during the following experiments. A simple block diagram of the designed tag architecture is shown in Fig. 21.
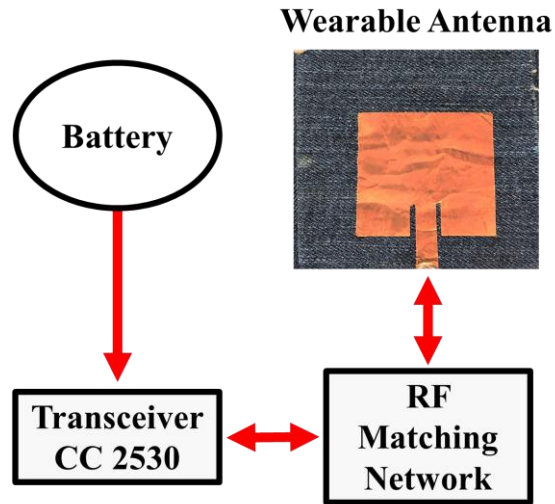

Fig. 21. Block diagram of the adopted RFID active tag (antenna realized on a denim substrate). [17] © 2019 IEEE

A typical laboratory scenario (schematically represented in Figs. 22) has been considered for this second set of measurements. Again, for the present case, $N_{EL}=N_{AZ}=3$, so that nine different sectors are used (9-zones calibration). For this environment, a path-loss exponent $n_{i,j}=1.4$ has been retrieved by means of calibration and considered in the following measurements and processing. The 3-D indoor localization measurements obtained for ten different tag positions randomly distributed are reported in Table IV and V (and represented in 2-D in Figs. 23 and 24, with the results obtained with denim double and triple layer tags, respectively),

together with the errors with respect to the real locations calculated as follows:

$$3D \text{ Error} = 100 \cdot \frac{\sqrt{(x_0-x_m)^2+(y_0-y_m)^2+(z_0-z_m)^2}}{\sqrt{x_0^2+y_0^2+z_0^2}} \qquad (10)$$

Every measurement has been obtained by averaging ten RSSIs with the tag located at the same tested point.

In this case, the reader is located at a 1.25-meter height from the ground, a suitable choice for detecting people standing, sitting, or falling.
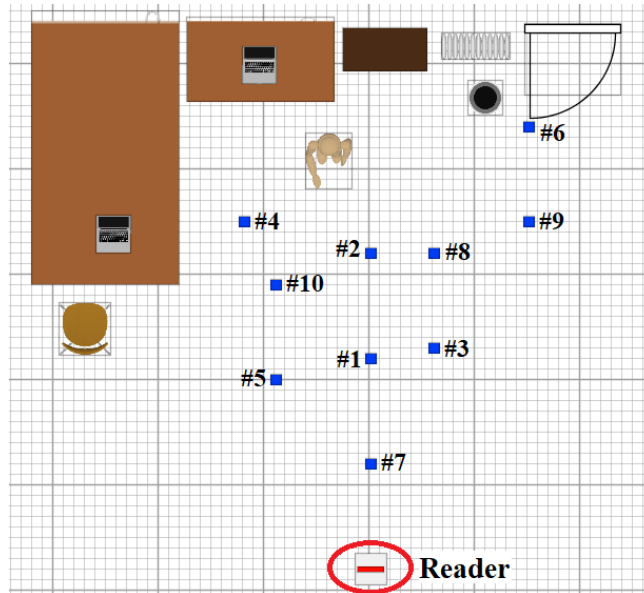
(a)
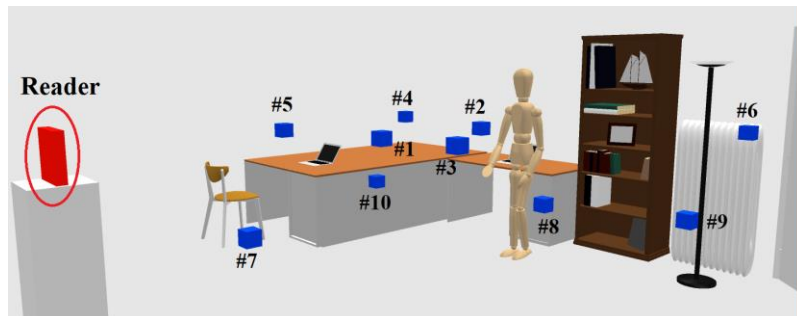
(b)

Fig. 22. (a) 2-D and (b) 3-D location of ten positions considered for the second set of localization measurements, with the RFID tags worn by the monitored users. [17] © 2019 IEEE

TABLE IV
RESULTS OF THE 3-D INDOOR LOCALIZATION MEASUREMENTS
(WEARABLE, DENIM DOUBLE LAYER TAG, THICKNESS=1.56 MM)

Point	Actual Position $(x_0;y_0)$	Measured Position $(x_m;y_m)$	Tag Height		3-D Error (%)
			Actual (z_0)	Meas. (z_m)	
#1	(5.45;2.00)	(5.47;1.86)	1.25	1.25	6.00
#2	(5.45;3.00)	(5.30;3.00)	1.25	1.25	4.62
#3	(6.05;2.10)	(6.07;1.95)	1.25	1.17	6.80
#4	(4.25;3.30)	(4.46;2.86)	1.25	1.38	13.54
#5	(4.55;1.80)	(4.70;1.53)	1.25	1.20	13.21
#6	(6.95;4.20)	(6.37;3.99)	1.25	1.02	14.21
#7	(5.45;1.00)	(5.40;0.92)	0.75	0.73	7.71
#8	(6.05;3.00)	(6.34;2.82)	0.75	0.77	10.85
#9	(6.95;3.30)	(6.45;3.63)	0.75	0.97	17.24
#10	(4.55;2.70)	(4.92;2.40)	0.75	0.67	16.41

All Cartesian coordinates and altitudes are expressed in meters. Reader height: 125 cm. The Reader distance from the bottom left corner of the room is 5.45 m. [17] © 2019 IEEE
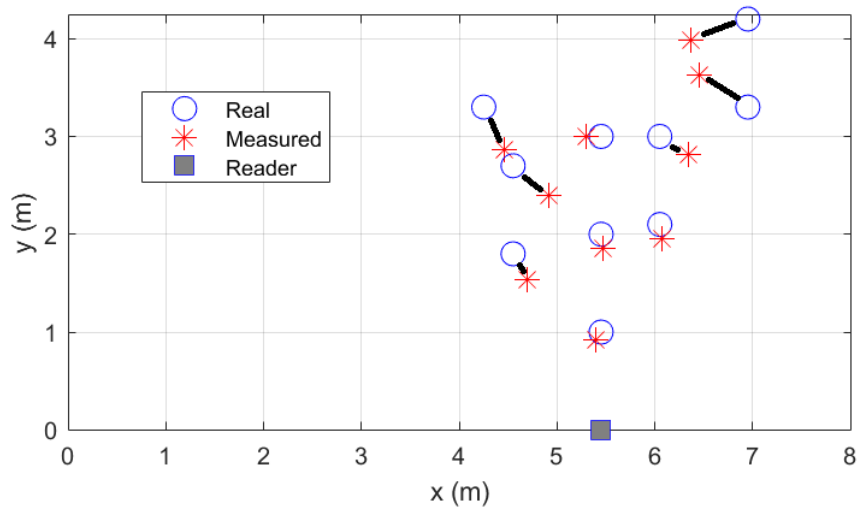

Fig. 23. Actual and measured bidimensional positions of the tagged user equipped with the denim double-layer wearable tag.

TABLE V
RESULTS OF THE 3-D INDOOR LOCALIZATION MEASUREMENTS
(WEARABLE, DENIM TRIPLE LAYER TAG, THICKNESS=2.34 MM)

Point	Actual Position $(x_0;y_0)$	Measured Position $(x_m;y_m)$	Tag Height		3-D Error (%)
			Actual (z_0)	Meas. (z_m)	
#1	(5.45;2.00)	(5.42;2,09)	1.25	1.25	4.02
#2	(5.45;3.00)	(5.50;2.95)	1.25	1.28	2.36
#3	(6.05;2.10)	(5.91;1.91)	1.25	1.09	11.33
#4	(4.25;3.30)	(4.50;3.42)	1.25	1.17	7.74
#5	(4.55;1.80)	(4.74;1.63)	1.25	1.15	11.56
#6	(6.95;4.20)	(7.25;4.09)	1.25	1.10	7.62
#7	(5.45;1.00)	(5.40;1.38)	0.75	0.55	34.59
#8	(6.05;3.00)	(6.18;3.06)	0.75	0.80	4.81
#9	(6.95;3.30)	(7.16;4.30)	0.75	0.78	27.62
#10	(4.55;2.70)	(4.61;3.18)	0.75	0.70	16.52

All Cartesian coordinates and altitudes are expressed in meters. Reader height: 125 cm. The Reader distance from the bottom left corner of the room is 5.45 m.
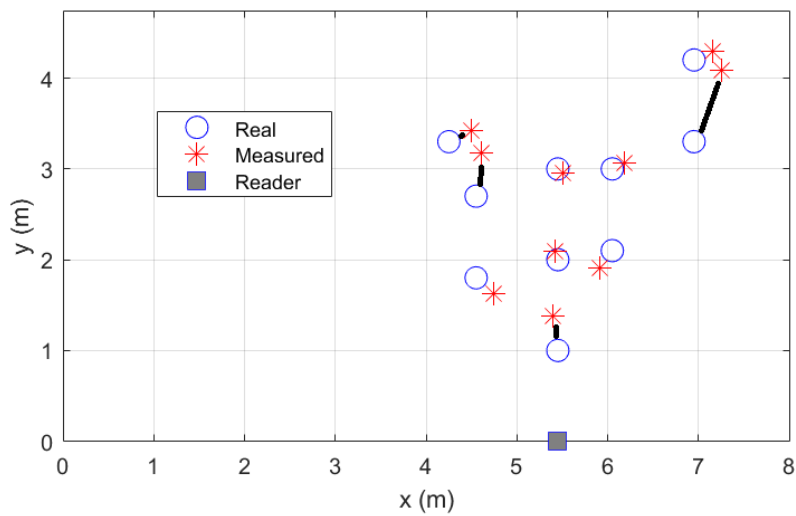

Fig. 24. Actual and measured bidimensional positions of the tagged user equipped with the denim triple layer wearable tag.

To assess the impact of the tag antenna, the same localization scenario of Figs. 22 has been tested using the commercial monopole antenna of the CC2530EM together with its evaluation board and comparing the results obtained with the two versions of the denim wearable antenna with different thicknesses, after performing a calibration for each of these three different situations (results are reported in Table VI): while with the commercial monopole tags an average error of 20.1 cm is observed for reader-tag distances lower than 2.60 m, the average error with wearable tags is less than 18 cm for distances up to 4.50 m.

TABLE VI
AVERAGE LOCALIZATION ERRORS FOR
THE THREE MEASUREMENT CAMPAIGNS

Adopted Tag	Tag Size	Average 2-D Error (x;y)	Average Height Error	Average 3-D Error
Commercial Tag (Antenna: TI CC2530EM Integrated Monopole)	165.3 cm^2	22.7 cm	15.0 cm	20.1 cm
Wearable Tag #1 (Antenna: Patch with Denim Double Layer)	90.9 cm^2	22.2 cm	8.3 cm	17.6 cm
Wearable Tag #2 (Antenna: Patch with Denim Triple Layer)	93.3 cm^2	20.3 cm	8.5 cm	16.4 cm

Finally, the system performance has been tested in presence of two tagged people moving in a room; the tracked trajectories are depicted in Fig. 25, whereas the corresponding measures and position percentage errors are reported in Table VII. They have been moving for 30 seconds, starting from the positions labeled with t_0, and their measured locations

have been compared with the effective ones, which are reported in the same figure: even when the two people were close by, the average 3-D positioning error was under control, for the required system specifications to track people activities in a room.

TABLE VII
DYNAMIC LOCALIZATION MEASUREMENTS IN PRESENCE OF TWO PEOPLE
(WEARABLE, DENIM TRIPLE LAYER TAG, THICKNESS=2.34 MM)

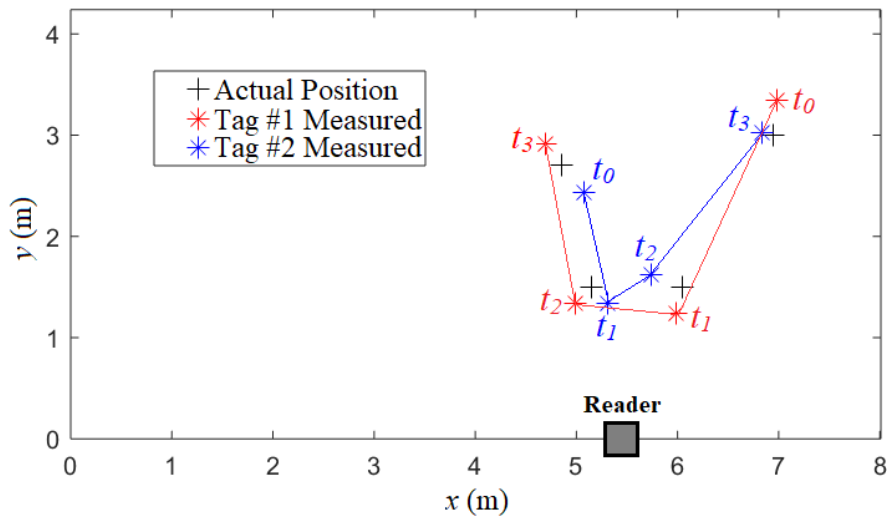| Point	Actual Position $(x_0;y_0)$	Measured Position Tag #1 $(x_{m1};y_{m1})$	Measured Position Tag #2 $(x_{m2};y_{m2})$	2-D Error Tag #1 (%)	2-D Error Tag #2 (%)
#1	(6.93;3.00)	(6.98;3.34)	(6.84;3.02)	10.18	3.33
#2	(6.05;1.50)	(5.98;1.24)	(5.74;1.62)	16.67	20.58
#3	(5.15;1.50)	(5.31;1.34)	(5.31;1.34)	14.79	14.79
#4	(4.85;2.70)	(4.70;2.91)	(5.08;2.43)	9.33	12.82

Fig. 25. Actual and measured positions of two tagged people moving in the indoor environment during a walk of about 30 seconds. t_0 is the starting position for each person. [17] © 2019 IEEE

The presented RFID reader has been designed also to detect potential falls that could occur to people living alone in indoor environments. Exploiting the elevation scanning capability of the reader and its monopulse radar technique, it is possible to notice whenever a tag is fallen or rather positioned on the floor, thanks to the information provided from the MPR_{EL} pattern whose maximum values correspond to the detected elevation of the tags. Moreover, when the tagged person has fallen, his height is lower than the reader one, resulting in a lower RSSI than the one expected when a person is standing: this is possible to be detected by the reader and an alert for remote falls can be activated; Figs. 26 and 27 represent the aforementioned conditions, showing Σ, Δ_{EL}, and MPR_{EL} for two different falling detections of a user wearing the tag, at a 1-meter and 3-meters distance from the reader, respectively; it is possible to notice that for the first situation, the tag is out of the calibrated elevation zone of the reader of [-45°, 45°], but the system is still able to detect the low tag height, although the MPR_{EL} shows a plateau in the [-45°, -30°] zone instead of a sharp peak; conversely, for the tagged user lying down at 3-meters distance, the MPR_{EL} maximum peaks is located at -30°, corresponding to the actual angular position of the active tag in the elevation plane.
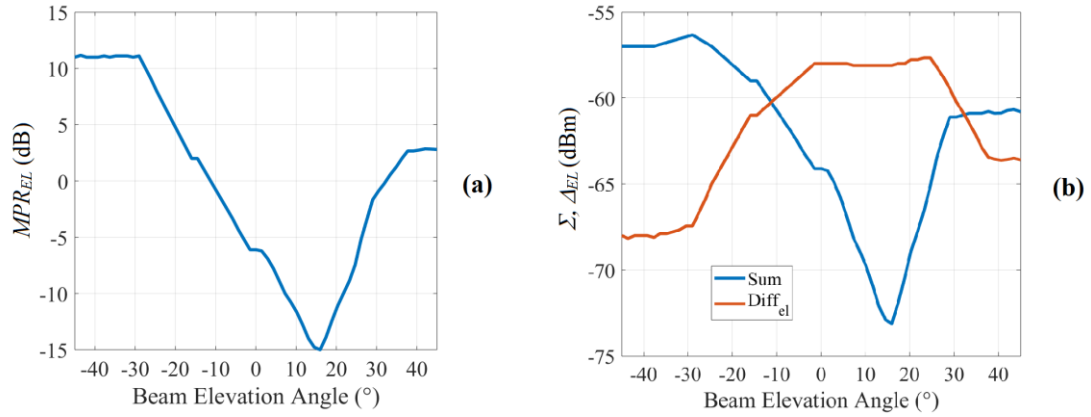
Fig. 26. Diagrams of (a) MPR$_{EL}$, (b) Σ, and Δ$_{EL}$ in the elevation plane achieved after the fall of a tagged user at 1 meter of distance from the reader. [17] © 2019 IEEE
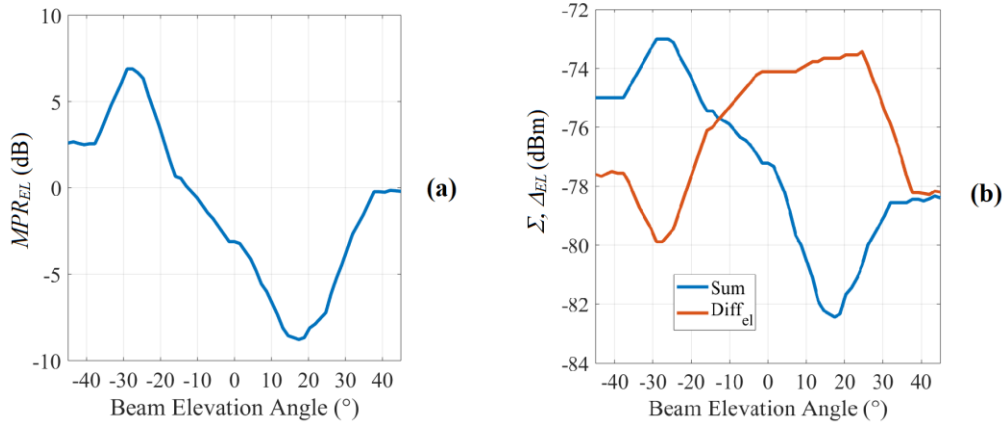

Fig. 27. Diagrams of (a) MPR$_{EL}$, (b) Σ, and Δ$_{EL}$ in the elevation plane achieved after the fall of a tagged user at 3 meters of distance from the reader. [17] © 2019 IEEE

Similar results have been obtained for other fall detection experiments in the same indoor scenario of Figs. 22: twelve different fall episodes have been tested and verified: i) lying down face upwards (Fig. 28 (a)); ii) lying down face downwards; iii) lying down lateral (on both sides); iv) sitting (Fig. 28 (b)), all with reader-tag distances of 0.5, 2 and 3 meters; these measurements always led to correct detection of the fall events, with no false positive or false negative situations, demonstrating that the

present microwave system can be a reliable solution to detect falls of elderly people living alone, in communities or cohousing, thus getting rid of continuous assistance. A further advantage of this proposed fall detection sensor is that it operates alone and in real-time and the reader operations take less than 15 seconds to be completed.

Moreover, the system can be embedded in everyday life objects and wirelessly connected to a smart-home platform augmented with decision-making algorithms to activate the proper alarm for the proper person.
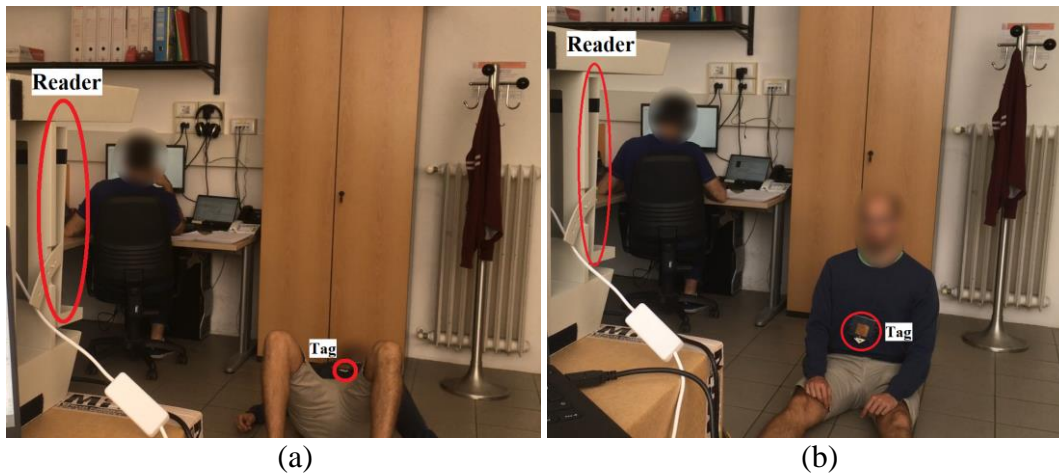
Fig. 28. Pictures of two potential situations detectable with the reader capabilities: (a) the person is lying down face upwards; (b) the person fell down sitting. [17] © 2019 IEEE

A 5.8 GHz Self-Injection Locked Oscillator for Breath Detection

This chapter is based on the following publications:

G. Paolini, M. Feliciani, D. Masotti, and A. Costanzo, "Experimental Study of a Self-Oscillating Antenna at 5.8 GHz for Breath Monitoring," IEEE-APS Topical Conference on Antennas and Propagation in Wireless Communications (APWC), Granada, Spain, pp. 198-200, 2019. © 2019 IEEE

G. Paolini, M. Feliciani, D. Masotti, and A. Costanzo, "Toward an Energy-Autonomous Wearable System for Human Breath Detection," 2020 International Microwave Biomedical Conference (IMBioC), Toulouse, France, pp. 1-3, 2020. © 2020 IEEE

G. Paolini, Y. Murillo, S. Claessens, D. Masotti, S. Pollin, A. Costanzo, and D. Schreurs, "RF Energy Harvesting from GFSK-Modulated BLE Signals," IEEE Topical Conference on Wireless Sensors and Sensor Networks (WiSNet), San Diego, CA, USA, pp.1-3, 2021. © 2021 IEEE

3.1. Architecture and Principles of Operation of the Wearable SIL Radar

This section presents the design and the experimental studies of a 5.8 GHz SILO for vital signs detection, in particular human breath, working without the need of any anchor nodes nor remotely synchronized receivers. Specifically, the prototype used for this scope exploits the two cross-polarized EM fields of an aperture-coupled fed patch antenna representing the typical input and output ports of a SILO structure. The overall working principles of this device consist in the reception of the FM signal coming from the user's chest moving under the effect of

breathing. Moreover, this device can be considered fully wearable, i.e., worn by the user in the chest position inside a plastic case assuring a suitable distance from the body. Finally, in addition to the respiratory rate, a tentative estimation of the lung capacity is also feasible, with a distinction between the normal and deep breath.

A. SILO Architecture and Principles of Operation

The fundamental radiating element of the presented sensor is the two-aperture-coupled patch antenna at 5.8 GHz shown in Fig. 29 (a) and presented in [56]: the chosen dielectric substrate is Neltec NY9208 (ε_r=2.08, thickness: 1.524 mm), whereas the feeding network and the oscillator circuitry (Fig. 29 (b)) are realized on a Taconic RF60-A (ε_r=6.15, thickness: 0.635 mm).

The ground plane is interposed between the two dielectric substrates and presents two orthogonal slots (dashed lines in Fig. 29 (a)) allowing the EM coupling between the microstrips and the antenna and, consequently, the feeding of the antenna itself. The microstrip feeding lines and the slots are positioned in such a way that the sensor can provide two orthogonal linear polarizations at the two ports of the oscillator.
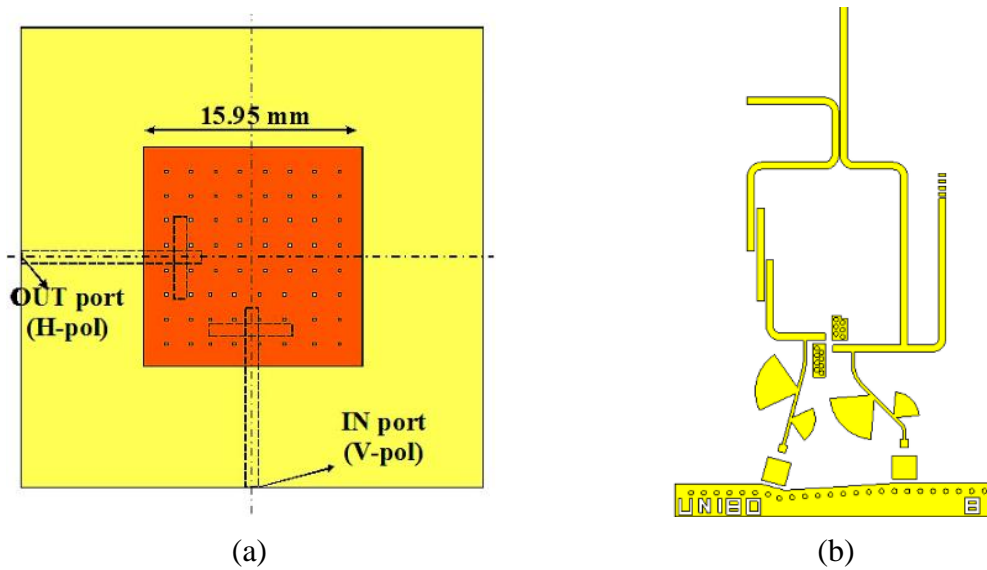
Fig. 29. (a) Front view of the sensor with patch antenna; the slots placed in the ground plane and the microstrip feeding lines placed in the bottom layer are shown with dashed lines. (b) Back view with the RF and DC circuitries and the orthogonal microstrip feeding lines. [26] © 2019 IEEE

The aim of this research concerns breath monitoring through this wearable oscillator using the injection-locking theory. Since the radiant element and the oscillator circuit strongly interact with each other, being the antenna part of the feedback loop of the oscillator, the design of the self-oscillating active antenna is particularly challenging; therefore, nonlinear circuit techniques combined with EM analysis methods were used to realize the present configuration.

The SILO configuration presents two ports: through the output port, the signal is sent to the subject, whereas through the other one (input port for injection locking), the oscillator gets into a SIL state by receiving the signal reflected by the body and collected by the receiving instrumentation. Therefore, the oscillator must be able to manage two

cross-polarized signals: the output signal horizontally polarized and the input signal vertically polarized, in the present case. The orthogonal polarizations at the two ports are achieved through non-resonating orthogonal slots etched on the ground plane. To enhance both dual-polarized behavior and a high decoupling between input and output ports, a hole-shaped topology of the patch metallization was adopted, thus reaching good matching and good isolation. A DC generator is used to bias the pseudomorphic high electron mobility transistor (PHEMT) of the oscillator circuit: for the present case, the drain and gate voltages are set to V_D=3.7 V and V_G=0.6 V, respectively. This choice has been derived by the oscillator stability analysis [56] ensuring an unstable DC bias and a stable RF oscillation. The predicted RF output power is 13 dBm.

B. Experimental Studies for Human Breath Detection

The measurement campaign previewed the characterization of the sensor worn by four different subjects, placing the SILO sensor in a plastic case (Fig. 30) at a 2.5-cm distance from the subject's chest.

The subjects were standing in front of a horn antenna (TDK Horn: 1-18 GHz) connected to the spectrum analyzer (Agilent N1996A: 100 kHz-6 GHz), i.e., the receiving section of the measurement setup, at a distance of 1, 1.5 and 2 meters.

Fig. 30. Photograph of the SILO prototype worn by the user under test. [26] © 2019 IEEE

The subjects were asked first to hold their breath for few seconds to register the free-running oscillator frequency; subsequently, they performed normal breathing for 50 seconds, followed by 10 seconds of a deep breath. Fig. 31 shows the pattern representing the typical trend of the locking frequency of the oscillator registered during the tests for a subject at a 1-meter distance from the receiver.
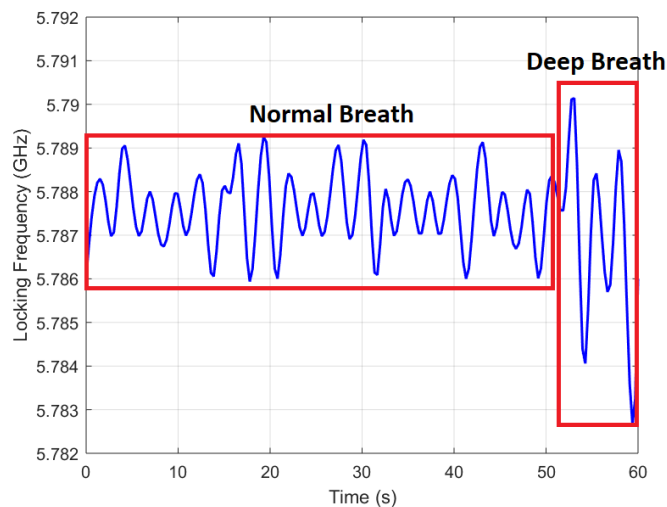

Fig. 31. Evolution of the SILO locking frequency during a test over a period of 1 minute. [26] © 2019 IEEE

Through these measurements, the feasibility of the system has been verified: specifically, it has been noticed that the range of the locking frequency varies for each subject and depends also on the distance from the receiving antenna: in particular, during inspiration/expiration, it is possible to notice an increase/decrease of the oscillator locking frequency, respectively; the largest differences in terms of widening of the locking frequency range result in conjunction with a deep breath exercised by the subjects under test, as it is possible to notice in Table VIII and Figs. 32; substantial differences have also been detected for subject #3 (woman), compared to the other three (men).

In order to evaluate the effects of non-ionizing radiations of the SILO tag, the effective isotropic radiated power (EIRP) and the specific absorption rate (SAR) were calculated, referring to the limits established by the Federal Communications Commission (FCC) and the International Commission on Non-Ionizing Radiation Protection (ICNIRP). Considering a transmitted power and an antenna gain of 13 dBm and 6.84 dBi respectively, for the oscillator under exam, the EIRP value calculated is equal to 17.34 dBm (approximately 54 mW), also considering the cable losses. The SAR value was mediated on a 10-g volume of a multi-layer model made of dielectric biological tissues (skin, fat, and muscle) by using the EM simulation software CST Microwave Studio; the maximum 10-g volume averaged SAR value resulted to be equal to 0.44 W/kg,

hence within permitted values established by the abovementioned
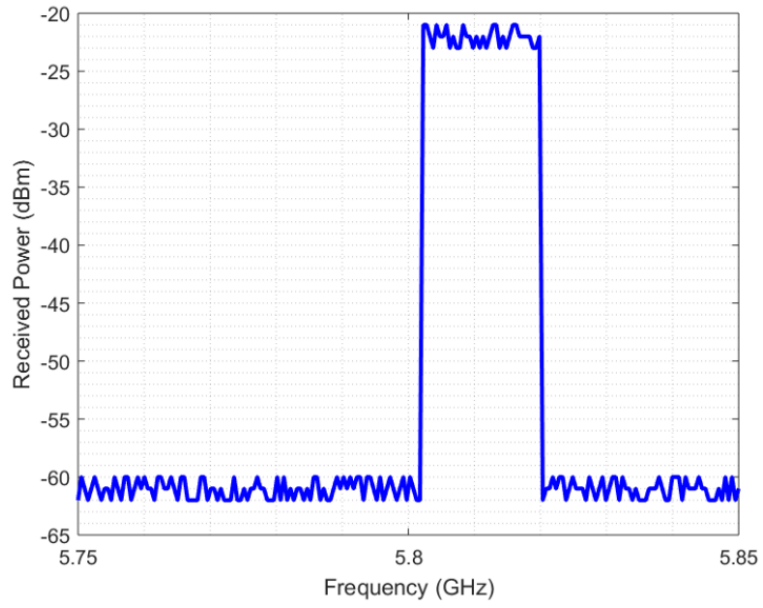
regulatory bodies.

TABLE VIII
LOCKING FREQUENCY RANGE DURING BREATHING TESTS ON
FOUR DIFFERENT SUBJECTS AT 1.5 METERS FROM THE RECEIVER

Subject	$\Delta f = f_{max} - f_{min}$	
#1	4 MHz	10 MHz
#2	7 MHz	10 MHz
#3	9 MHz	19 MHz
#4	4 MHz	10 MHz

[26] © 2019 IEEE
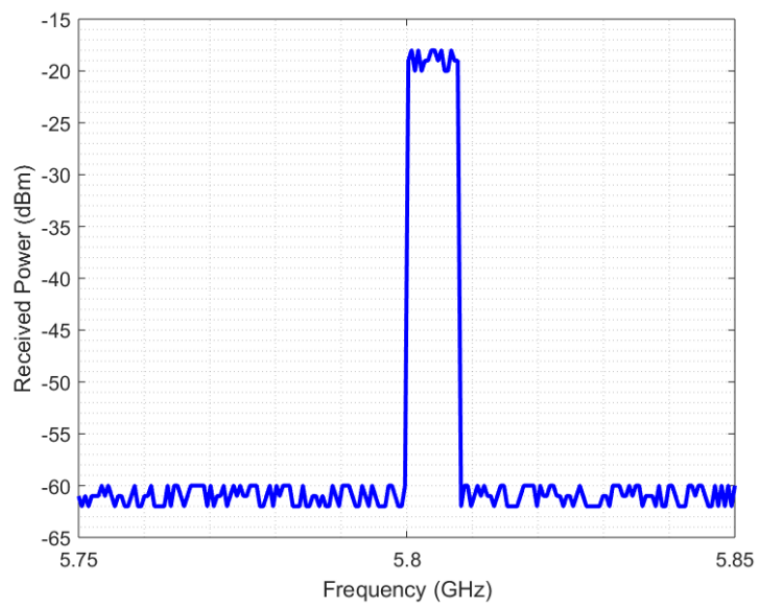
(a)

(b)

Fig. 32. Signal-processed graphs showing the SILO locking frequency spanning for subject #3 during (a) normal breath and (b) deep breath at the distance of 1.5 m from the horn antenna. [26] © 2019 IEEE

3.2. Simultaneous Wireless Information and Power Transfer for Breath Detection

Once the SILO has transmitted the RF wave, the reflected one is phase, frequency, and amplitude modulated by the chest movements; thus, the baseband signal can be acquired by frequency or amplitude demodulation techniques.

In [57], a similar system is proposed where the SIL and the frequency demodulation can be realized by means of integration and derivation sub-circuits. Indeed, the first-order differentiator straightforwardly allows to derive the time variations of a biomedical signal; the differentiator output is then connected to an active peak detector and a baseband amplifier.

Conversely, in this new presented design, the demodulation procedure is carried out by adopting a fully passive peak detector of the signal, modulated by the user's chest displacement, in addition to an RF-to-DC rectifier to harvest part of the incoming power, in order to achieve a proper simultaneous wireless information and power transfer (SWIPT).

A. First Design of Integration of a Passive Peak Detector and an RF Energy Harvester

The peak detector circuit schematic, including the component values, is reported in Fig. 33: its load is chosen equal to 2.3 kΩ, emulating a

Bluetooth commercial chip that can be connected afterward to receive the detected data, i.e., the breath rate.
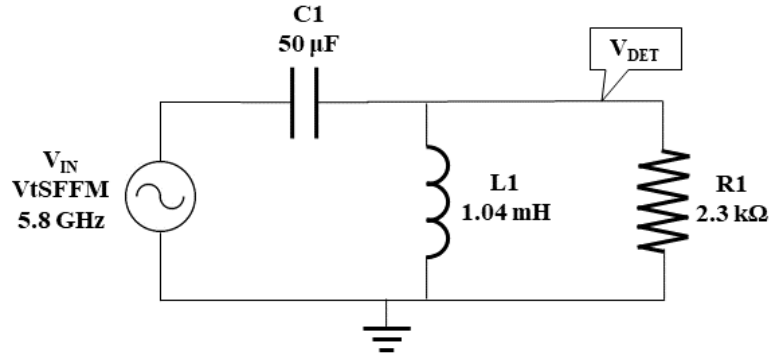

Fig. 33. Circuit schematic of the peak detector to be weakly coupled to the SILO output with the aim of detecting the breath rate of the subject under evaluation. [58] © 2020 IEEE

As shown in Fig. 33, the output SILO signal is received by the detector and is represented as an equivalent voltage source (V_{IN}), and the whole circuit is simulated using the circuit simulation software Keysight ADS: V_{IN} is described by an FM voltage source (VtSFFM), with a carrier frequency of 5.8 GHz. The frequency modulating signal, which describes the breath rate (i.e., 0.27 Hz for 16 breaths/min), is chosen with a modulation index h equal to:

$$h = \frac{\Delta f}{f_m} \tag{11}$$

where Δf is the maximum deviation of the instantaneous frequency from the carrier frequency (about 10 MHz for normal breath, see Fig. 32 (a)), and f_m is the highest frequency component belonging to the modulating signal.

With the aim of further exploiting the same RF SILO output to power supply a Bluetooth radio placed on-board of the sensor, a voltage-doubler rectifying circuit at 5.8 GHz has been designed and placed downstream of the peak detector.

The typical circuit schematic of the full-wave RF-to-DC rectifier [59], including the values of the passive components, is represented in Fig. 34. The two diodes are the Skyworks SMS7630-079LF; the rectifier load is R_{LOAD}=0.51 kΩ, representing the optimum load for a buck-boost DC/DC converter (i.e., TI bq25570), that has to be chosen due to its specific behavior for harvesting energy from low-voltage, low-power sources (down to 100 mV and 15 µW).
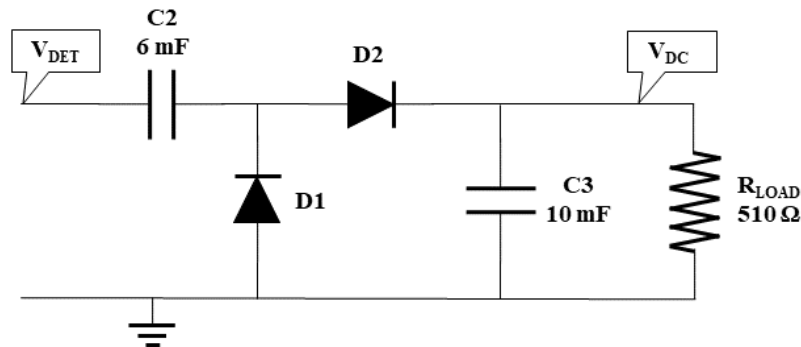

Fig. 34. The layout of the voltage-doubler rectifier at 5.8 GHz. [58] © 2020 IEEE

First, an ADS transient simulation of the system of Fig. 33 is carried out, with an ideal sinusoidal voltage source of amplitude V_{IN}=0.35 V at 5.8 GHz, frequency-modulated by a signal with h=10˙000 and f_m=1 Hz, to emulate realistic tachypnea in adult subjects (typical values: from 30 to 60 breaths/min).
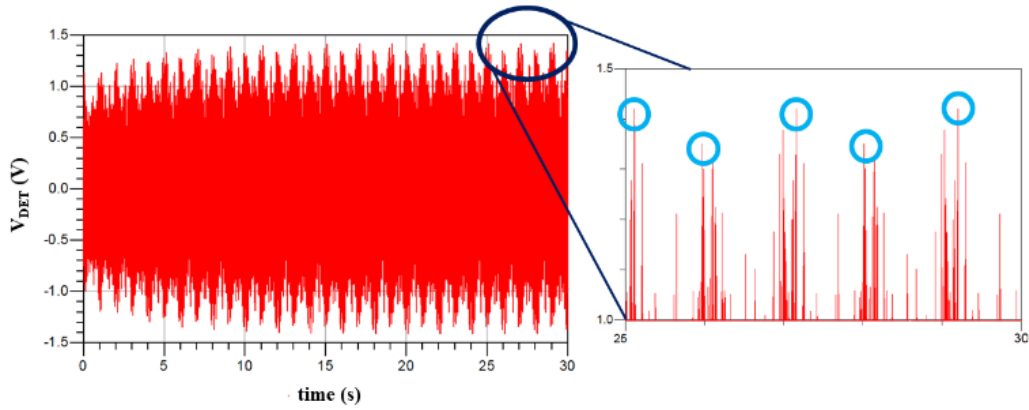
Figs. 35 show the waveforms of V_{IN} and V_{DET} respectively, for a time duration of 30 seconds. In this case, for every period (1 second) of the modulating signal, it is possible to notice two peaks, one for the inhalation and one for the exhalation, which have been highlighted in Fig. 35 (b) in order to demonstrate that the adopted topology is able to detect the breath rate at 1 Hz.
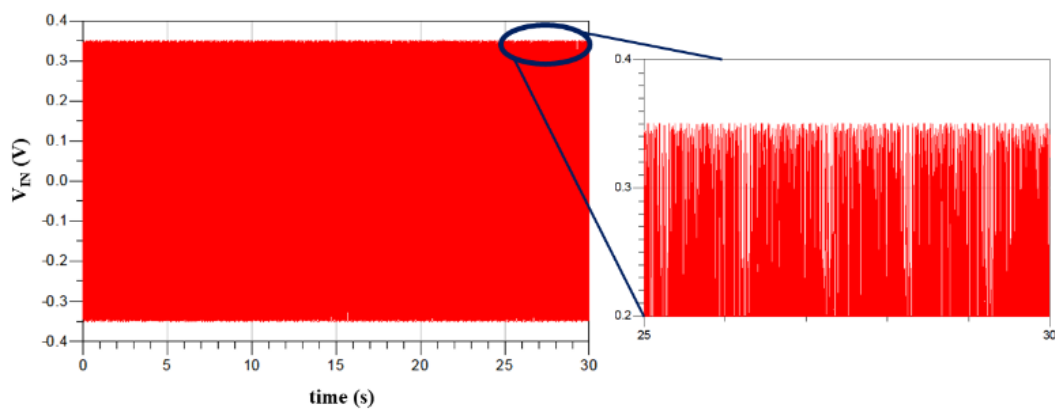
(a)
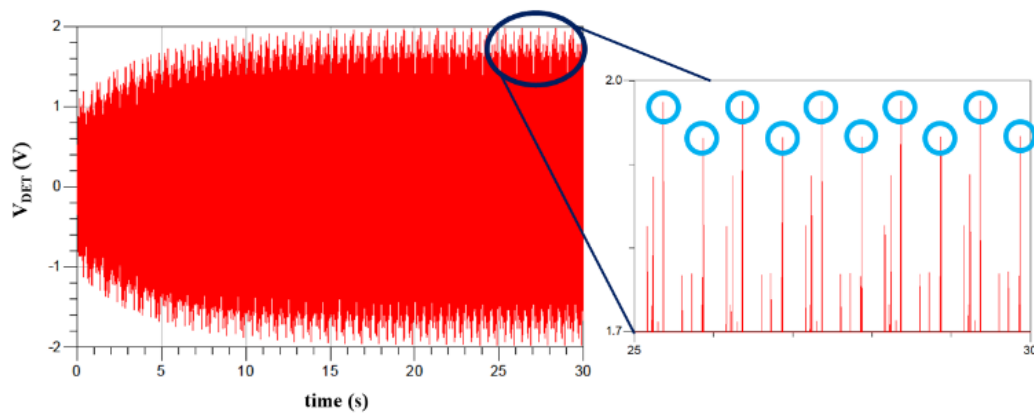
(b)

(c)

Fig. 35. Simulated behavior of (a) V_{IN}, and V_{DET} for a transient simulation of 30 seconds and considering a modulating signal (breath) of (b) 1 Hz and (c) 0.5 Hz. The callouts show the difference between the waveforms of V_{IN} and V_{DET} for detecting the peaks of the modulated signal, corresponding to inhalations and exhalations. [58] © 2020 IEEE

The same situation occurs for a respiratory rate of 0.5 Hz (30 breaths/min), as it is possible to distinguish from the peaks in the last five seconds of the simulation reported in Fig. 35 (c).

It is worth mentioning that the callouts for the last 5 seconds are shown in order to emphasize peaks that can however be noticed also for the previous 25 seconds of the simulation.

In a second step, to predict the EH capabilities of the proposed system, the peak detector is loaded by the rectifier and the whole system is analyzed in steady-state conditions, by means of the harmonic balance (HB) technique with the same sinusoidal excitation spanning the frequency band of interest (from 5.79 to 5.81 GHz) covered by the modulated signal representing the breath rate. No significant performance

variations have been observed all over the band. The predicted DC output power is 7.6 dBm, for an RF input power of 10 dBm, resulting in an RF-to-DC efficiency of 57.8%. Similar results have been obtained by the time-domain simulation of the whole circuit, under modulated conditions: in this latter case, the computed DC output power is 7.4 dBm.

In particular, considering the breath rate at 1 Hz, a V_{DC} of 1.68 V and a P_{DC} of 5.5 mW are obtained after a transitory time of 15 seconds, perfectly in line with the minimum levels enabling the operation of modern buck-boost DC/DC converters.

As regards information concerning ADS simulation times, the HB simulation with four harmonics took only 5.38 seconds, whereas a transient simulation of 30 seconds (maximum time step: 1 ms) lasted 7 seconds.

B. Toward a Conception of a Single Circuit for SWIPT

The previous section of this chapter described the design of a 5.8 GHz SILO for vital signs detection, in particular human breath, achieved through a peak detector and an RF-to-DC rectifier, a circuit to be connected to the output port of the wearable oscillator through a microstrip coupled line (Fig. 36).
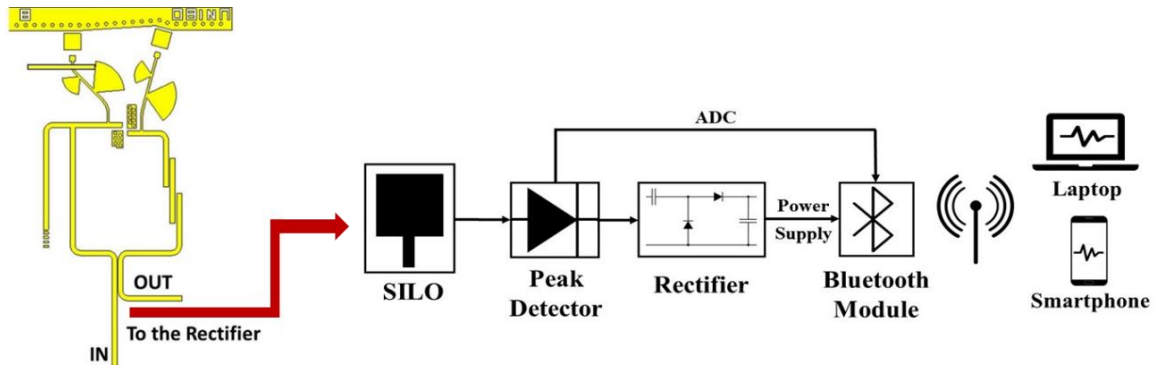
Fig. 36. Block diagram of the wearable prototype for breath detection, with the SWIPT circuitry connected to the oscillator output port.

The following steps preview the project of a single circuit able to harvest the RF energy at 5.8 GHz coming from the signal modulated by the human chest and, at the same time, to down-convert it into the baseband signal containing the information related to the variation of the injected frequency, hence the respiratory rate of the subject under test.

The new version of the circuit presents a typical version of the voltage-doubler rectifier consisting of two Schottky diodes (Skyworks SMS7630-079LF), two 10 µF Murata RF capacitors, and a resistor (R_{LOAD}=261 Ω) acting as a load.

By means of HB simulations performed by Keysight ADS, the rectifying performance has been predicted and reported in Fig. 37.

It is also possible to notice that for the measurements at the highest power (P_{IN}=10 dBm), the voltage-doubler power conversion efficiency (PCE) results to be about 36%, whereas 20% with 0 dBm of input power. These power levels are in line with the energy consumption of a

commercial control board (i.e., the Nordic Semiconductor Bluetooth module nRF52840), to be employed without the need of a dedicated battery.

It is worth noticing that the above-mentioned values of PCEs are lower than the ones reported in the literature because, in this case, the matching network is missing, a necessary condition observed in the ADS transient analysis to properly detect the peaks in correspondence of every inhalation/exhalation.
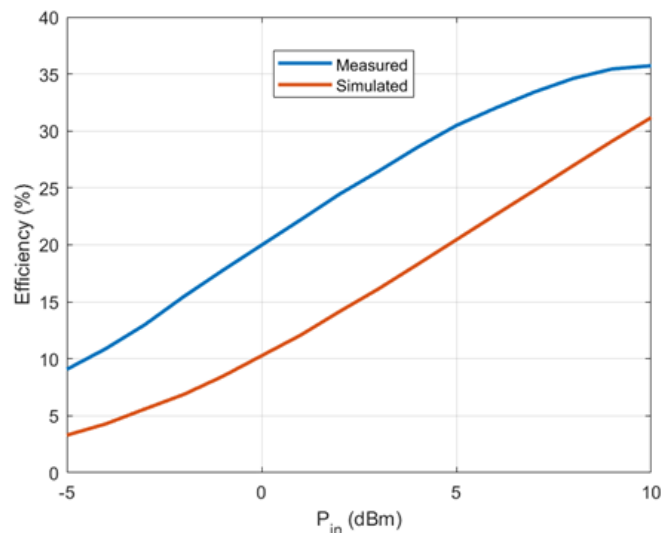

Fig. 37. Simulated and measured power conversion efficiencies are shown for the voltage-doubler rectifier circuit.

The parameters used in the ADS transient simulations are:

- total simulated time: 3 s, max step time: 1 µs.

- Source: voltage source, single frequency, frequency-modulated, with its waveform in time represented in Fig. 38 (a).

- Carrier frequency: 5.8 GHz, input power: 10 dBm.

- Modulating signal frequency (breath rate): 1 Hz.

- Maximum deviation of the instantaneous frequency from the carrier: 10 MHz.

- Modulation index: h=10˙000˙000.

The application of an FM signal at 5.8 GHz representing the signal generated by the oscillator and then reflected by the chest, resulted in the peaks detection shown in Fig. 38 (b), in this case, every second (see the modulating signal frequency adopted for the transient simulation).

It is possible to notice that in this case the peak value (inhalation) is at 848 mV and the next peak stands 48 mV behind (exhalation); for a half-wave rectifier, this difference is about 26 mV, meaning that the detection of the correct breath frequency is more difficult in this last case; this is the reason why the voltage-doubler layout has been preferred, besides the fact that it reaches better PCEs.
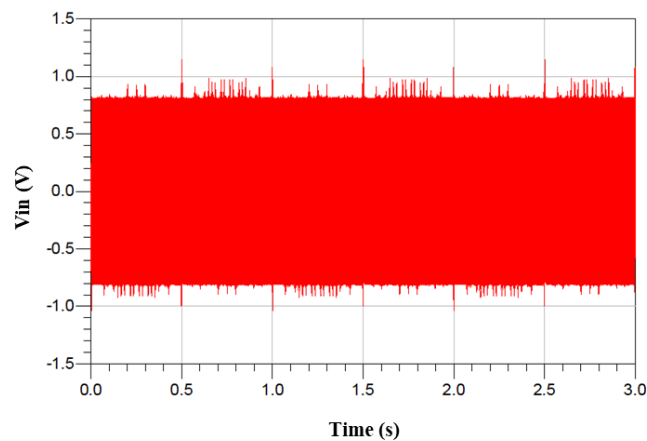
(a)
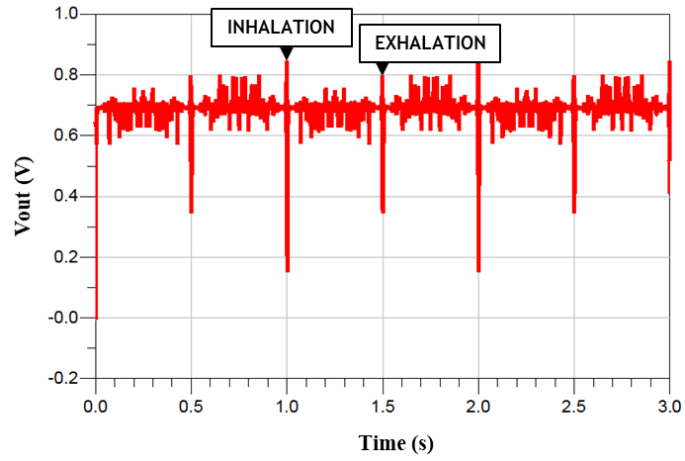
(b)

Fig. 38. Voltage waveforms of (a) the input FM signal with the carrier at 5.8 GHz, and (b) baseband signal at the output of the voltage-doubler rectifier.

3.3. Energy Harvesting and Data Transfer with Frequency Modulated Input Signals

Intending to further investigate the possibility of harvesting RF energy from modulated signals, this section presents an experimental study on the feasibility of EH from wireless signals that are present normally in daily life environments, i.e., BLE.

First, the design of the RF-to-DC conversion circuit is presented, considering the input excitation being a signal modulated in frequency.

Finally, a measurement campaign has been conducted considering as input signal both an FM excitation given by a signal generator and the real communication packets sent by a commercial Bluetooth board.

A. Design of the Rectifying Circuit for FM Signals

The design of the rectenna (rectifying antenna) to be included in an envisioned battery-less sensor node previews the presence of an antenna and an RF-to-DC rectifier in order to harvest the energy coming from modulated signals. Its block diagram is fully described in Fig. 39.
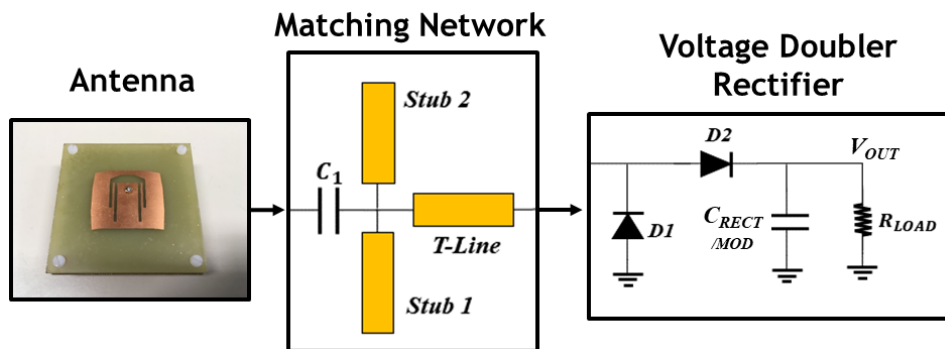

Fig. 39. Block diagram of the rectenna used for EH operations. [60] © 2021 IEEE

The antenna selected for EH is a multi-band patch with a gain of 6 dBi in the 2.4 GHz band [61], with coaxial feeding to be connected to the RF-to-DC rectifier, which is a voltage-doubler composed of an input matching network (a 1 pF Murata RF capacitor (C_1), two 50-Ω open stubs in parallel, and a 50-Ω transmission line in series), two Schottky diodes (Skyworks SMS7630-079LF), one Murata RF capacitor ($C_{RECT/MOD}$), and a resistor (R_{LOAD}) acting as load and setting the cut-off frequency (f_{co}) of the output low-pass filter. The final layout of the rectifier, comprising of the matching network, is represented in Fig. 40.
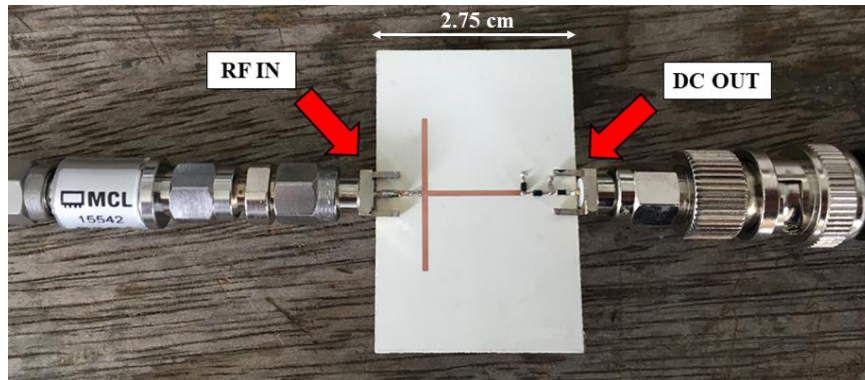

Fig. 40. Picture of the board realized for BLE-harvesting purposes. [60] © 2021 IEEE

Frequency-modulated excitation, typical for BLE packets, has been considered in the simulations with Keysight ADS [62]. In particular, the excitation consists of a two-level Gaussian frequency shift keying (2-GFSK) modulation, with a data rate equal to 1 Mbps and bandwidth-period product (BT) of 0.5. This means that the bandwidth (BW) of the Gaussian filter has to be 0.5 MHz.

The key elements to generate a proper 2-GFSK signal, using a gaussian-filtered pseudo-random bit sequence, are: i) single-frequency voltage source, considering an input power of -10 dBm for this case, emulating the power level that can be reached under these conditions; ii) FM modulator: RF carrier and modulating signal generating the modulated signal (sensitivity: 1 MHz); iii) voltage source, pseudo-random pulse train (bit rate: 1 Mbps); iv) voltage-controlled voltage source (Z-domain); v) Gaussian low-pass filter, with BW=0.5 MHz.

In this research, the main goal is to investigate the feasibility of harvesting energy from an FM source, but also consider the possibility to demodulate the BLE signal itself at the rectifier output without the need of a local oscillator (LO), and thus realizing the paradigm of SWIPT.

For this purpose, it is notable to refer to the waveforms obtained at the rectifier output (V_{OUT} in Fig. 39), whose voltage and efficiency as a function of time (30 μs-simulation) are reported in Figs. 41, as well as the input voltage V_{IN}. At the output, the same circuit topology has been used to realize two low-pass filters, with f_{co}=25 kHz for WPT, and f_{co}=2 MHz for SWIPT of a 1-Mbps-data-rate signal, using two different output capacitances (C_{RECT}=1 nF and C_{MOD}=12 pF, respectively).
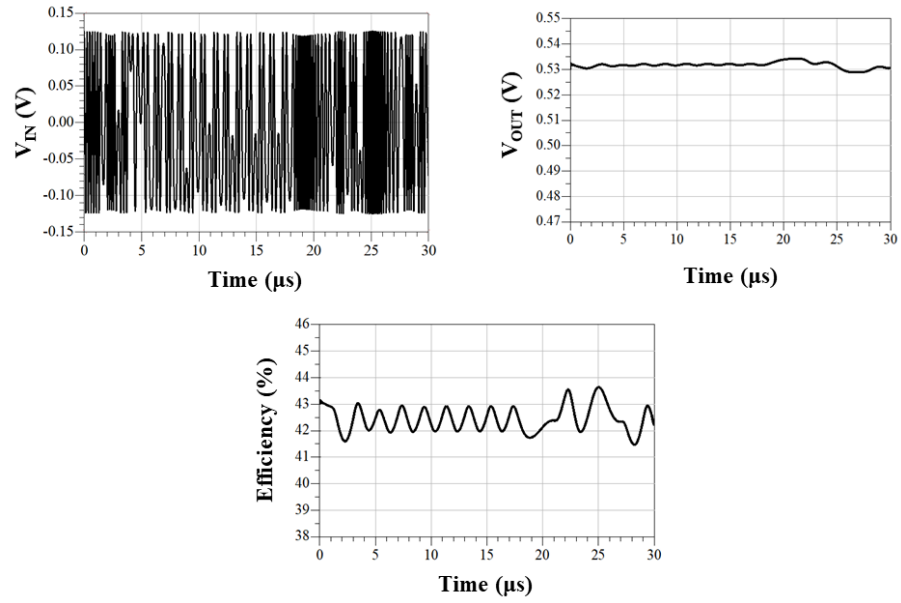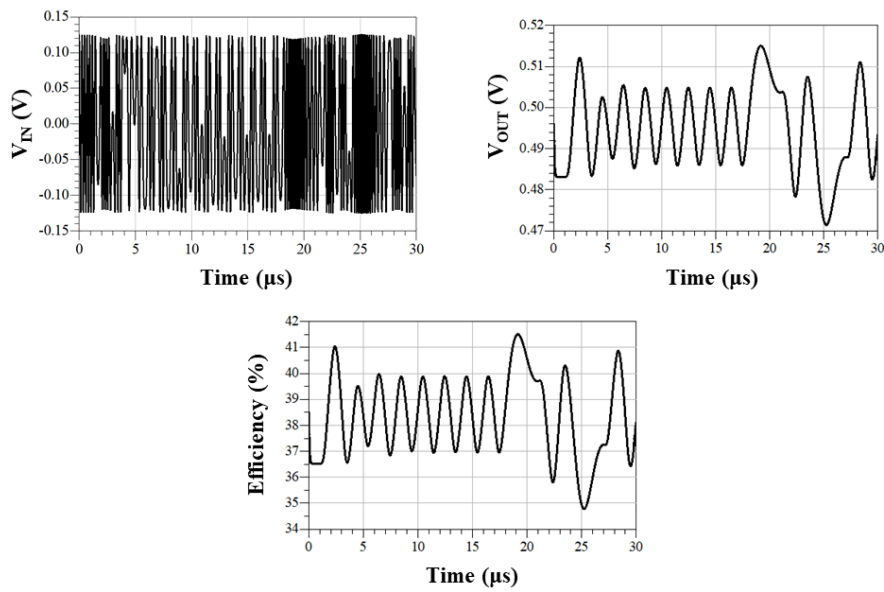
Fig. 41. Input voltage, output voltage, and efficiency for the presented rectifier, with the bandwidth of the output filter set in order to achieve (a) a pure WPT, and (b) SWIPT (f_{co}=2 MHz). [60] © 2021 IEEE

Fig. 42 represents the simulated and measured PCEs obtained with a single tone at 2.426 GHz (BLE advertising channel #38) and applying a 2-GFSK signal centered at the same frequency (generated by an E4438C ESG vector signal generator), respectively, with a sweep of the input power from -20 to 5 dBm. In this case, it is possible to notice the quasi-total superposition between the results obtained by harvesting a single tone and an FM signal.
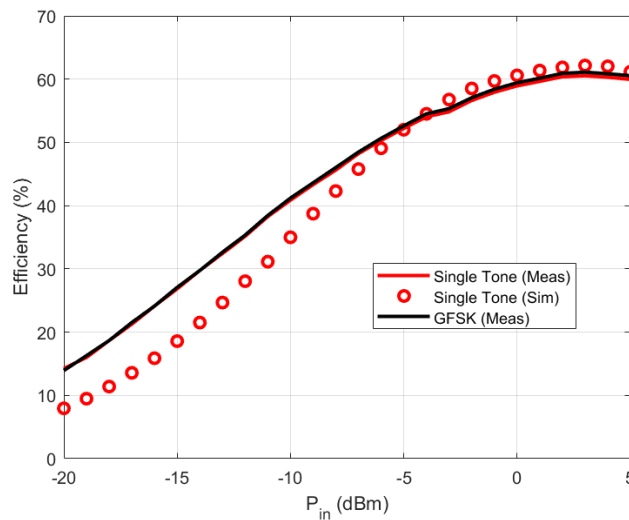

Fig. 42. Simulated and measured PCEs for a single tone and a 2-GFSK excitation. [60] © 2021 IEEE

The following step involved the programming of the BLE commercial board nRF52840 from Nordic Semiconductor, in order to send Bluetooth advertising packets every 10 ms. Fig. 43 represents the adopted

measurement setup, with the BLE board acting as a transmitter and the rectenna as a receiver.

The goal, in this case, is to investigate the possibility to harvest RF energy directly from a real communication signal, without the need for a dedicated continuous wave (CW) source, as it is done in most cases for WPT.
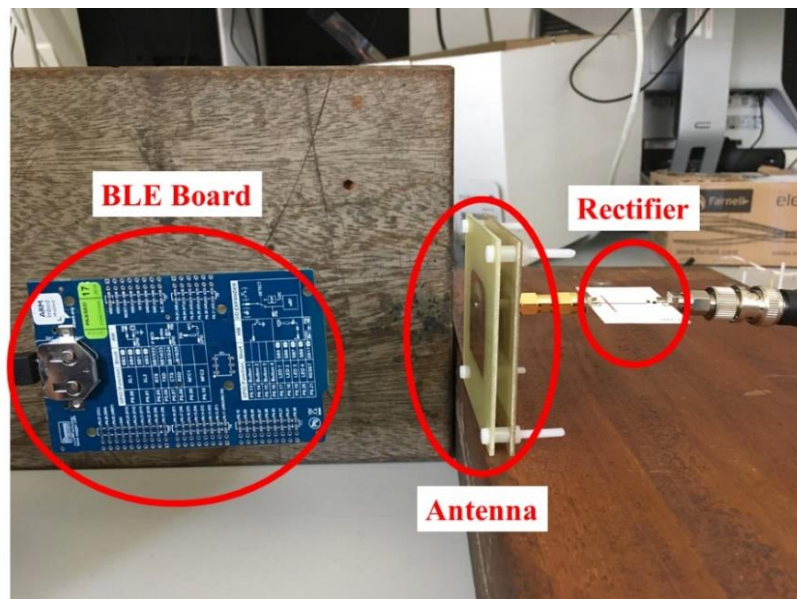
Fig. 43. Measurement setup for the experimental study of EH from FM signals coming from a commercial BLE evaluation board. [60] © 2021 IEEE

Table IX summarizes the distances (although not in far-field) from the BLE board to the receiving rectenna, and the corresponding open-circuit voltages obtained at the rectifier output, with the Bluetooth board transmitting 4 dBm.

Finally, a tentative energy budget estimation (for one packet) has been carried out, which is reported in the third column of Table IX, assuming a

packet duration of about 300 μs, a 50%-efficiency for the power management unit (PMU) and adopting the actual measured rectifier efficiencies reported in Fig. 42 for the GFSK signal.

TABLE IX
MEASURED OPEN CIRCUIT VOLTAGE AND ESTIMATION OF AVAILABLE
ENERGY FOR DIFFERENT TRANSMITTER-RECEIVER DISTANCES

Distance	Open Circuit Voltage	Harvested Energy
1.8 cm	3 V	54 nJ
4.2 cm	2 V	25 nJ
9.5 cm	1 V	6.2 nJ
19.4 cm	0.5 V	1.3 nJ
36.0 cm	No rectified voltage	---

[60] © 2021 IEEE

A WPT-IoT System for Predictive Maintenance in Electromagnetically Harsh Industrial Environments

This chapter is based on the following publications:

G. Paolini, M. Shanawani, A. Costanzo, F. Benassi, and D. Masotti, "RF Energy On-Demand for Automotive Applications," IEEE MTT-S International Microwave Symposium (IMS), Los Angeles, CA, USA, pp. 1191-1194, 2020. © 2020 IEEE

G. Paolini, M. Guermandi, D. Masotti, M. Shanawani, F. Benassi, L. Benini, and A. Costanzo, "RF-Powered Low-Energy Sensor Nodes for Predictive Maintenance in Electromagnetically Harsh Industrial Environments," Sensors, vol. 21, no. 2, pp. 386-403, Jan. 2021.

4.1. Design of RF Power Sources at 2.45 GHz and Low-Power Wireless Sensor Nodes

This chapter proposes the design and the realization of a custom WPT system operating in the 2.4 GHz band for remote monitoring, predictive maintenance, and diagnosis of components allocated in the engine compartment of a car. The system is composed of one or more RF sources, called illuminators, and a multitude of wireless sensor nodes placed in key points of the engine compartment, in close contact with the parts of the car that need to be monitored. Through this research, it has been demonstrated that the sensors can be correctly powered without the need for a battery and simultaneously communicate with a gateway in order to register, in a given amount of time, the acceleration and the

temperature registered by the sensors corresponding to a given part. The communication of the gateway with the sensor nodes takes place exploiting the LoRa protocol working in the same frequency band of the RF powering system. In this way, it is possible to prevent or register possible malfunctioning, failure, or unwanted warming of the tagged components.

A. 2.45 GHz RF Illuminator Design and Realization

The illuminator circuitry has been realized by using off-the-shelf components, namely Maxim MAX2750 voltage-controlled oscillators (VCO), having an output power of -3 dBm in the 2.4 GHz ISM band; this frequency band selection has been chosen in order to have small size antennas both at the illuminator and at the sensor node side.

The adoption of a VCO allows to dynamically select the illuminators operating frequency to enable frequency division between the powering and the communication operations. The VCO tuning voltage input is given by a voltage control element (Linear Technology LT6650) that is set to have the oscillator signal at 2.45 GHz; this choice has been made with the aim of having sufficient distance in the spectrum between the WPT signal and the LoRa communication signal (at 2.401 GHz).

The other key elements of the illuminator are the RF amplifiers incoherently feeding the antennas; the selected component is the

Skyworks SE2598L, having a gain of 26 dB and therefore able to ensure an output power of 23 dBm at the transmitting circularly polarized (CP) patch antennas; hence, having measured a 4 dBi-gain for the antennas, the total EIRP for each illuminator channel is 27 dBm, compliant with current regulations.

Circular polarization has been chosen to ensure robust WPT performance to the sensors regardless of their rotation with respect to the incident EM waves, and it has been obtained by means of the corner-trimming technique. Fig. 44 shows the values of the axial ratio at 2.45 GHz for each of the illuminator antennas, which is lower than 5 dB for azimuthal rotations in the ±100° range.
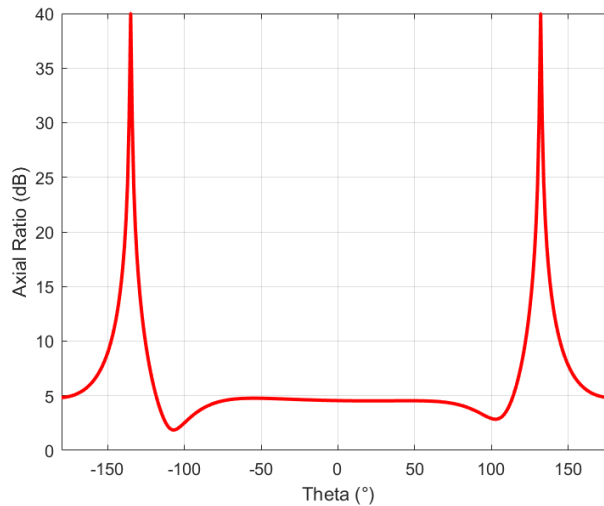

Fig. 44. The pattern of the axial ratio calculated for the transmitting antennas of the illuminator.

The chosen substrate for the board is Rogers RO4360G2 (thickness: 0.610 mm, with ε_r=6.15, tan(δ)=0.0038), in order to have a reduced microstrip line width of 0.9 mm for a 50-Ω impedance and at the same

time low dielectric losses, with respect to a standard FR4 substrate (ε_r=4.3, tan(δ)=0.025).

On the other hand, three CP patch antennas are reached by right-angle coaxial connectors and they are realized on a thicker and less dense Rogers RO4350B (thickness: 1.524 mm, with ε_r=3.48, tan(δ)=0.0037).

The entire board of the RF source is shown in Figs. 45, including the three CP antennas rotated by 45° one from each other. The overall dimensions of the illuminator prototype are 13 x 6 x 5.5 cm^3.


(a)
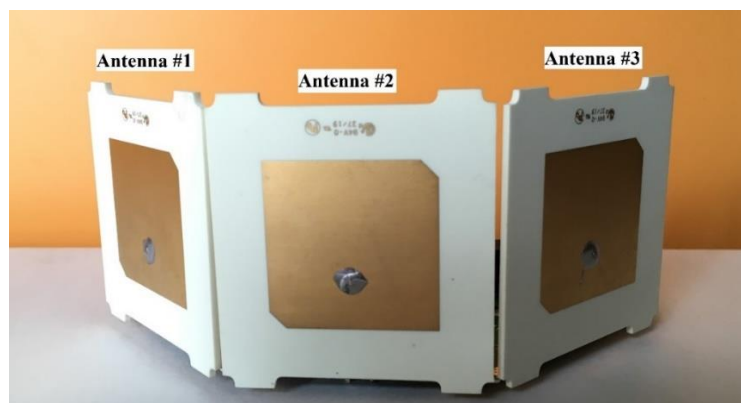
(b)

Fig. 45. (a) Picture of the illuminator feeding circuitry working in the 2.4 GHz band. (b) Front view with the three coaxial-fed CP patch antennas. [46] © 2020 IEEE

Figs. 46 show the simulated normalized radiation patterns of the self-standing three antennas (Fig. 46 (a)) and the normalized total radiation pattern (measured and simulated) due to the incoherent and simultaneous feeding strategy of the antennas (Fig. 46 (b)), both in the horizontal plane.
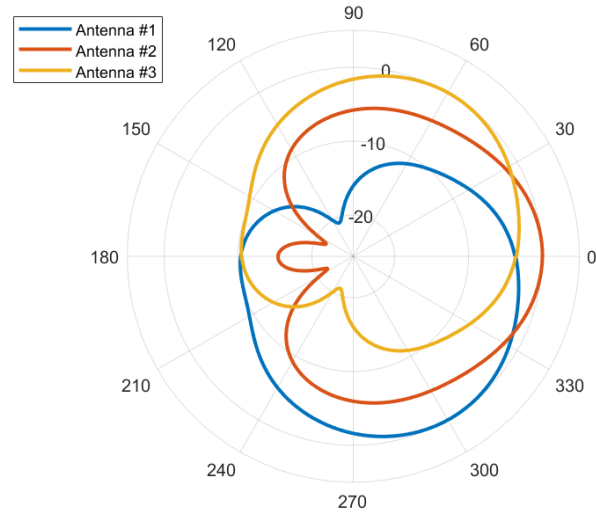
(a)
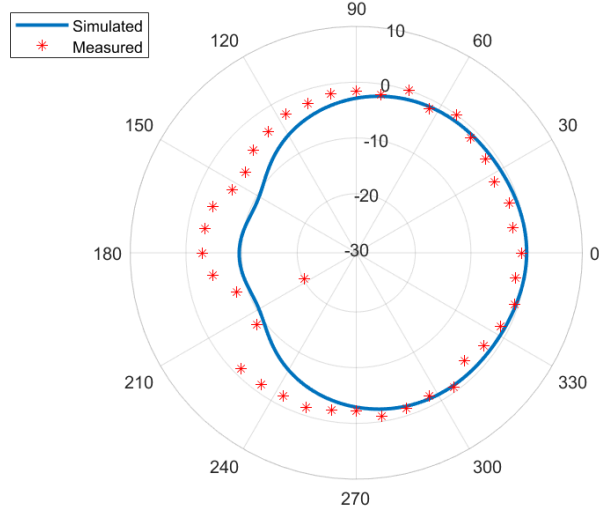
(b)

Fig. 46. (a) Normalized simulated polar patterns (in dB) of the self-standing three illuminator CP patch antennas and (b) normalized simulated and measured polar patterns of the entire RF illuminator, both in the horizontal plane. [46] © 2020 IEEE

B. Design of Low-Power Wireless Battery-Less Sensor Nodes

The 3-D implementation of the whole tag has been conceived with the twofold goal of miniaturization and insulation from metallic environments. The top layer consists of the radiating elements, whereas the bottom layer hosts the RF-to-DC rectifier, the radio, and the baseband subsystem for power managing purposes, except for two energy storage capacitors that are located on the top layer in order to reduce the overall node thickness.

The radiating part is shown in Fig. 47 and is located on the top layer. It operates in the 2.4 GHz band, for both communication and powering, and consists of two separate antennas, to allow SWIPT and to avoid the excess energy consumption of an RF switch, that could degrade the EH operations.
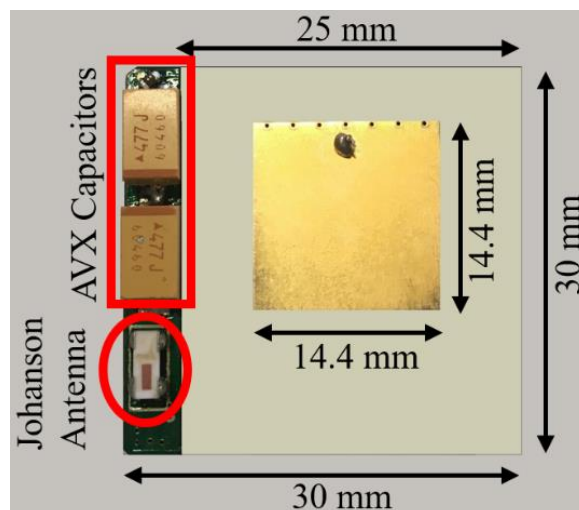

Fig. 47. Top layer of the wireless sensor node: the miniaturized patch with shorted pins for EH, the metal mounted Johanson chip antenna, and the AVX storage capacitors are represented. [45]

For EH, a patch antenna miniaturized by means of (seven) shorting pins (Fig. 48) has been designed.
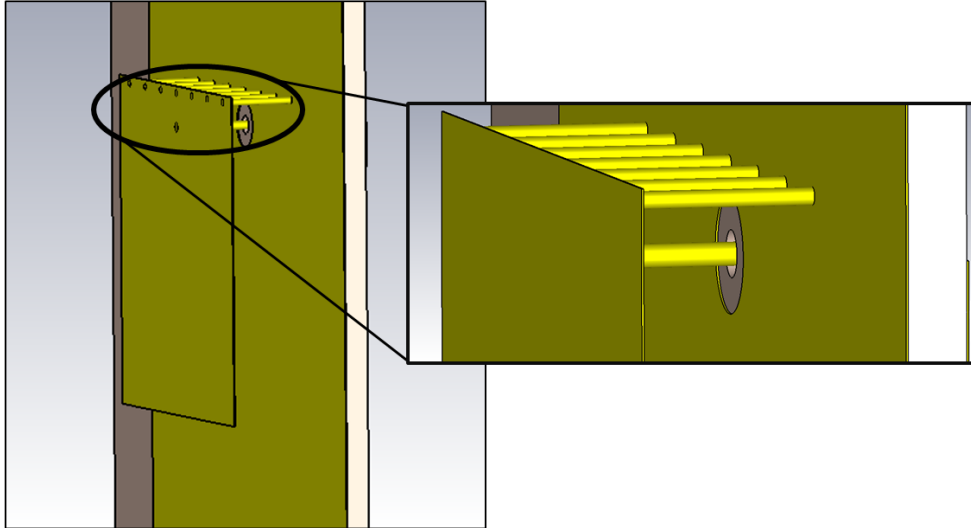
Fig. 48. The tridimensional layout of the designed miniaturized patch antenna top layer for RF energy harvesting.

To reduce the overall node dimensions, a coaxial-feeding technique has been chosen to connect the antenna to the rectifying circuit, which is located on the bottom layer together with the rest of the system circuitry. Using the Rogers RO4350B (thickness: 3.048 mm, ε_r=3.48, $\tan(\delta)$=0.0037) and the shorting pins technique, the antenna dimensions, including the substrate, are 2.5 x 3 x 0.32 cm^3, with a realized gain as high as 1.84 dBi, HPBW of 116°, radiation efficiency of 74%, and BW of 35 MHz. These performances have been predicted and measured despite about 50% antenna size reduction compared to a traditional patch antenna.

The communication operations are carried out by means of the Semtech SX1280 transceiver working in the 2.4 GHz ISM band. It is

worth noticing to observe that the choice to adopt two different antennas for WPT and communication is strategic to minimize energy losses, and in particular to avoid RF switches in the EH path. Whereas the performance of the WPT heavily depends on the radiation efficiency of the adopted antenna (which has been therefore custom designed), the communication based on LoRa has been proved to be robust to input signal levels as low as -132 dBm, largely achievable with the compact antenna, which is integrated on the node, i.e., a commercial surface mount technology (SMT) chip antenna (Johanson 2450AT42E0100, dimensions: 2 x 5 mm^2, thickness: 1.5 mm), specific for on-metal purposes. On the left side of the patch antenna substrate, an inset of 3.2 mm has been dug, in order to host the chip antenna without increasing the overall node thickness.

Mutual decoupling between the two co-located antennas placed in the same plane has been checked by measurements and is shown in Fig. 49 in terms of the transmittance parameter (S_{21}) of the resulting two-port antenna, showing good isolation (better than 20 dB in the two operating frequencies).
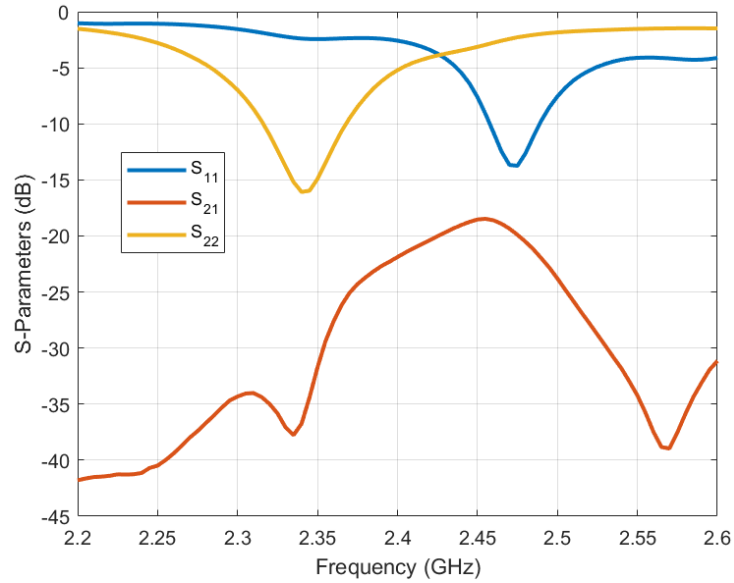
Fig. 49. Measured results of the scattering parameters of the two-port sensor node antenna: ports 1 and 2 correspond to the patch and the metal-mounted chip antenna, respectively.

C. Sensor Node Operations for LoRa Communication and Power Management

The block diagram of the whole WPT system is represented in Fig. 50, and the circuital implementation of the node is shown in Figs. 51.
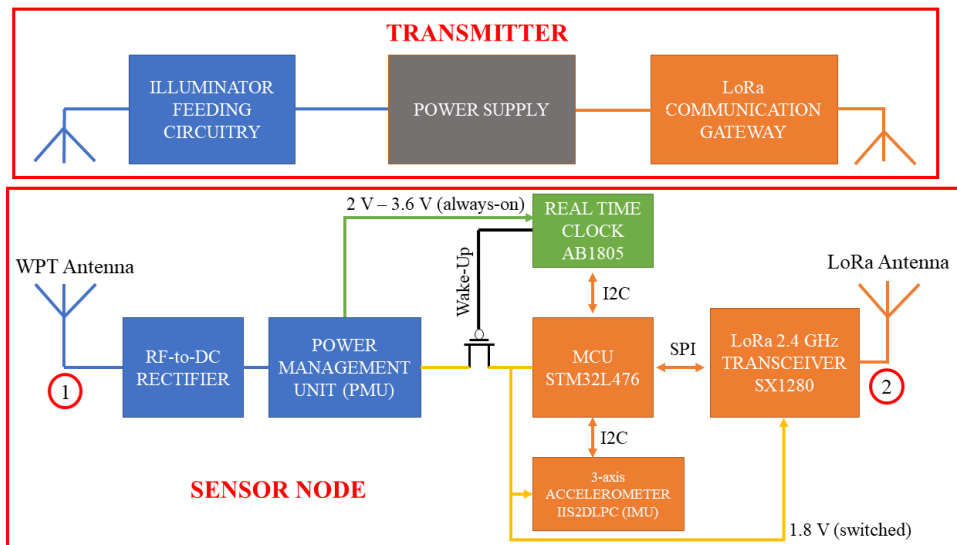
Fig. 50. Block diagram of the whole system: transmitter and wireless sensor node. [45]

97

In particular, the wireless sensor node is comprised of:

- two co-located antennas, operating in the same frequency band and adopting the frequency-diverse technique discussed above, one for receiving the energy to be harvested from the WPT, and one for communication.

- A full-wave rectifier, with a voltage-doubler (two Skyworks SMS7630-079LF diodes) and a matching network consisting of one 0.3 pF capacitor and a shorted stub (width: 0.51 mm; length: 5.7 mm), located at the top left of Fig. 51 (a), and connected to the top layer patch antenna port through a via hole (visible in Fig. 47). The predicted and measured performance of the rectifier in terms of PCE are reported in Fig. 52: although the behavior for increasing input power is very similar, simulations overestimate measurements until diodes breakdown occurs: this may be due to the diodes model, including the package parasitics used in the simulations that do not perfectly match their real behavior. The output of the rectifier has been connected to a buck-boost DC/DC converter (TI bq25570) specifically designed for harvesting energy from low voltage and low power sources.

- A power management section (including the bq25570) which efficiently controls the energy at the output of the rectifier to

charge two 470 μF ultra-low-leakage tantalum AVX capacitors that allow energy storage on the device and provide power supply to the node; these capacitors are quite thick and have been located on the top layer for 3-D miniaturization of the entire tag.

- A low power microcontroller unit (STMicroelectronics STML32476) to control the node peripherals.

- A 2.4 GHz SX1280 transceiver (Semtech Corporation) supporting LoRa communication protocol, feeding the 2450AT42E0100 (Johanson Technology) 2.4 GHz SMT above-metal mini chip antenna.

- An ultra-low-power 3-axis accelerometer (STMicroelectronics IIS2DLPC), or inertial measurement unit (IMU), for inertial sensing.

- An ultra-low-power real-time clock (RTC, Abracon AB1805) for duty-cycling the node operation by turning on the node at specific time intervals.
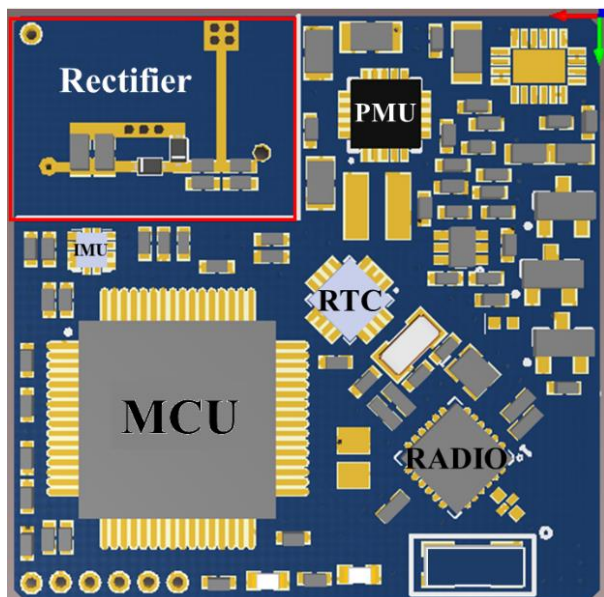
(a)
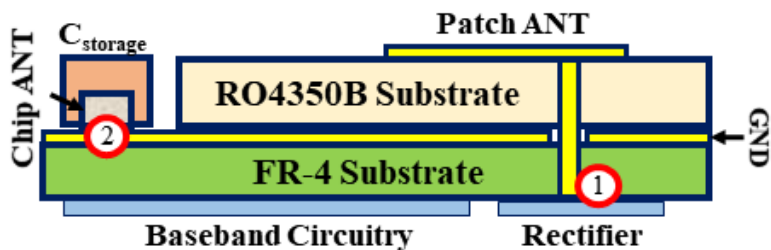
(b)

Fig. 51.　(a) The bottom layer of the sensor node, with highlighted the main components and the rectifier; (b) stack-up of the whole sensor node, with the antennas and the capacitors placed on the top layer, the RF and baseband components on the bottom, and the plated through-hole connecting patch and rectifier. [45]
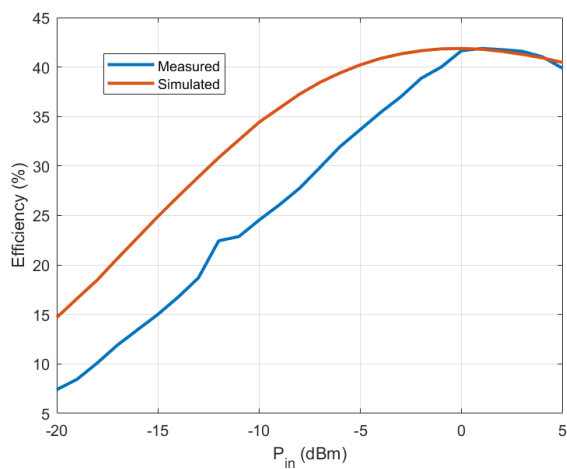
Fig. 52. Simulated and measured PCE of the sensor node voltage-doubler rectifier.

The node mostly operates in four phases (Fig. 53):

- *Start-Up*: when power is available at the input, but the storage elements are depleted, an undervoltage-lockout (UVLO) circuit keeps the load disconnected from the storage elements until it gets charged up to 2 V. During start-up, only charging operation occurs to minimize losses and charge time, and to avoid deadlock conditions, which could happen with an extremely low input power level.

- *First Power-On*: when the storage element voltage is above 2 V, the node turns on for the first time and transmits a short package to the gateway of the WSN to signal its presence in the system. The gateway replies with an acknowledgment. The MCU programs the RTC to wake up the node after the scheduled time. The RTC puts the node in an ultra-low-power sleep mode by cutting off the power supply to the load.

- *Sleep Mode*: only the RTC is on, with the node power consumption given by the RTC itself and the PMOS (p-type metal oxide semiconductor) load switch leakage currents. Overall current consumption is below 150 nA. The power management section keeps charging the storage element until it reaches the maximum voltage of 3.3 V.

- *Active Mode*: after the programmed sleep time has passed, the RTC awakes the node, and the MCU starts acquisition of accelerometer and temperature data over a 1-second window, processes it (for simplicity, only minimum, maximum, and average on the three-axis have been acquired in this example), and sends the data to the gateway. The gateway replies with an acknowledgment and, eventually, information on the next wake up time. The node programs the RTC and goes back to sleep mode until the RTC wakes it up again.

Transmission parameters for the LoRa radio are spreading factor 5, bandwidth 1625 kHz, code rate 4/5.
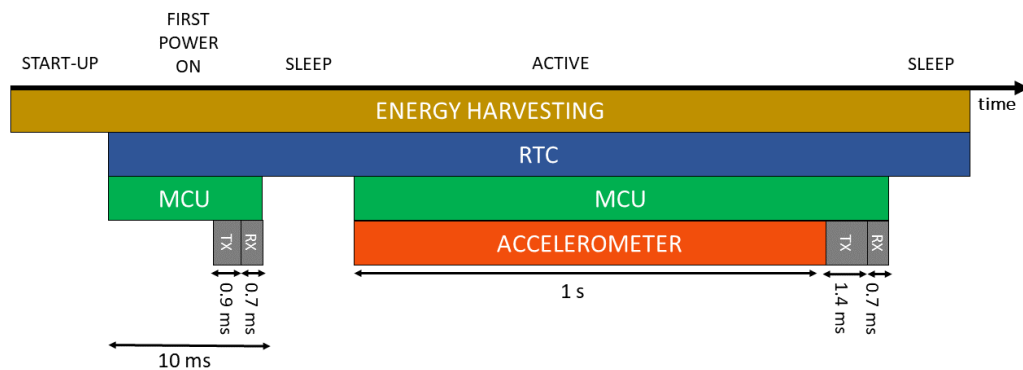
Fig. 53. Operational modes of the node, colours show which components are active in the different phases. [45]

Because of the limited amount of energy that can be harvested (down to few tens of µW), the storage elements need to present ultra-low leakage

currents. Typical leakage of rechargeable batteries, supercapacitors, and ceramic capacitors are not compatible with the requirements of the application. To overcome this issue, the storage element comprises two 470 µF ultra-low-leakage tantalum capacitors from AVX (TMJE447K), capable of limiting leakage to less than 2 µA.

The energy consumption of the different blocks of the node for two different sampling frequencies of the IMU data (400 samples per second (SPS) and 1600 SPS) have been characterized. Detailed energy requirements from the node components during the active mode cycle are presented in Table X.

TABLE X
NODE COMPONENTS AND CORRESPONDING
ENERGY DEMAND IN ACTIVE MODE

Component	Required Energy
MCU (400 SPS)	380 µJ
MCU (1600 SPS)	510 µJ
IMU (400 SPS)	265 µJ
IMU (1600 SPS)	275 µJ
LoRa Transceiver	405 µJ
Real-Time Clock	13.2 µJ

[45]

4.2. The Automotive Field Case Study: Validation Measurements in the Engine Compartment

Validation measurements regarding charging times and powers at stake have been performed adopting a static line-of-sight (LOS) channel on-air, in a typical RF laboratory environment with the presence of Wi-Fi and Bluetooth devices.

TABLE XI

REQUIRED TIMES FOR THE NODES TO FULLY CHARGE THE STORAGE CAPACITANCE FOR DIFFERENT DISTANCES AND INCLINATIONS IN FREE SPACE

Distance	Node Inclination	Charging Time
30 cm	0°	22 s
	30°	30 s
	45°	32 s
40 cm	0°	37 s
	30°	67 s
	45°	29 s
60 cm	0°	105 s
	30°	140 s
	45°	67 s
80 cm	0°	115 s
	30°	290 s
	45°	129 s
100 cm	0°	260 s
	30°	660 s
	45°	113 s

In Table XI, the measured results obtained during these tests in free space are reported, in terms of time for charging the storage capacitance up to 3.3 V (complete charge), for various orientations of the node with

respect to the maximum link direction, and for increasing power source-node distances from 30 cm up to 100 cm, which is from an almost near-field location up to the far-field condition.

Also, it was noticed that the maximum allowed distance from the illuminator to power the node is about 120 cm, confirming that the TI bq25570 cold-start takes place at 600 mV, at least.

Secondly, another set of measurements in free space has been conducted to characterize the maximum power point tracker (MPPT) operations of the TI bq25570 and to verify the accuracy of the ADS non-linear optimization carried out to maximize the efficiency of the rectifier in optimum loading condition, for a reference input RF power (here, chosen equal to -10 dBm, i.e., the targeted power reached inside the automotive environment).

TABLE XII
MEASUREMENT OF THE LOAD VALUES
EMULATING THE TI bq25570 MPPT OPERATIONS

| Illuminator-Node Distance	V_{OPEN}	R_{LOAD} @ $\frac{V_{OPEN}}{2}$
30 cm	3.24 V	7.58 kΩ
40 cm	2.12 V	10.43 kΩ
60 cm	1.58 V	12.38 kΩ
80 cm	0.92 V	9.40 kΩ
100 cm	0.66 V	10.20 kΩ

[45]

The open voltage (V_{OPEN}) at the output of the rectifier has been first measured; then, the rectifier DC output has been connected to a potentiometer in order to halve the open voltage, which is effectively how the MPPT of the PMU operates. The measured load values registered for $\frac{V_{OPEN}}{2}$ are reported in Table XII. It is worth noticing that for an illuminator-node distance of 80 cm, the open voltage is 920 mV, approximately corresponding to an input power of -10 dBm, which matches with a rectifier load (R_{LOAD}) of 9.40 kΩ, close to the optimum one predicted by the Keysight ADS optimizer (6.44 kΩ) for an input power of -10 dBm.

The final set of measurements has been carried out in the real scenario where this system is intended to be employed, namely the car engine compartment, with several sensor nodes placed in different engine locations and at different distances from the illuminator. The pictures of the two measurement setups are shown in Figs. 54 ((a) setup 1: the illuminator is up-frontal; (b) setup 2: the illuminator is down, left-sided), with six nodes distributed all over the engine compartment.

During these tests, a maximum node-illuminator distance of 112 cm has been considered. It is worth mentioning that sensor nodes are in this case placed in a quasi-total metallic environment which is affected by interfering reflections and non-line-of-sight (NLOS) propagation

conditions. Moreover, all the sensors are attached to metallic parts and, in most cases, are also placed close to other metallic elements of the engine.
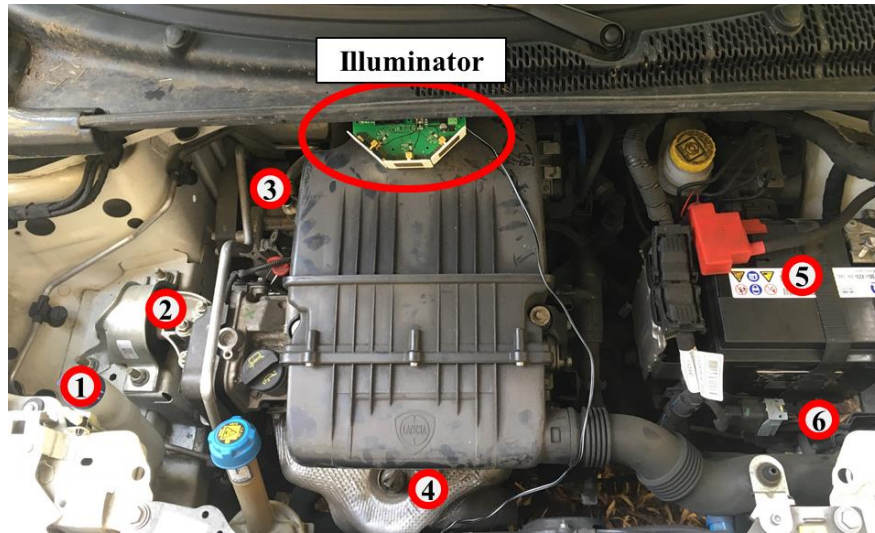
(a)

(b)

Fig. 54. Front and side views of the scenario under test. The RF illuminator and the six positions of the sensors are highlighted both for (a) setup 1 and (b) setup 2. [45]

The choice of their positions has been done in order to couple them with key elements of the engine and, at the same time, to cover all the

sectors in which the engine compartment can be sectorized. During these measurements, the bonnet was closed, and the instrumentation was placed outside the car, for the best mimic of realistic operations.

Six positions of the wireless sensor nodes in the abovementioned environment have been tested, tagging the most important parts that require parameters monitoring over time, such as acceleration and temperature, that can be detected by the node.

The presented system is going to operate in a harsh environment, also in terms of temperature. The main components of the prototypes offer storage and operating temperatures high enough (i.e., MAX2750 oscillator storage temperature: 150°C; bq25570 operating temperature: 125°C), whereas others (i.e., SE2598L amplifier) recommend operating temperature conditions below 85°C.

For these reasons, both the illuminators and the tags will be included in cases made of thermoplastic materials characterized by low thermal conductivity (k), e.g., PU (polyurethane) or ABS (acrylonitrile butadiene styrene), whose k are 0.025 and 0.25 W/(m·K), respectively, in order to minimize the heating of the circuits.

For what concerns the impact of the temperature on the properties of the antenna substrate (Rogers RO4350B), i.e., at 150° C the variation of its dielectric constant is limited to 0.4% and has no significant impact on detuning effects and losses of the antenna efficiency.

Figs. 55 (a) and (b) represents a summary of each sensor node's charging times for the two setups. In particular, three noteworthy charging times (end of cold-start, first power-on, and full charge) have been monitored, reporting the node-illuminator distance computed along a straight line, together with the minimum sleep time between two subsequent turn-ons of the node (minimum sleep interval).
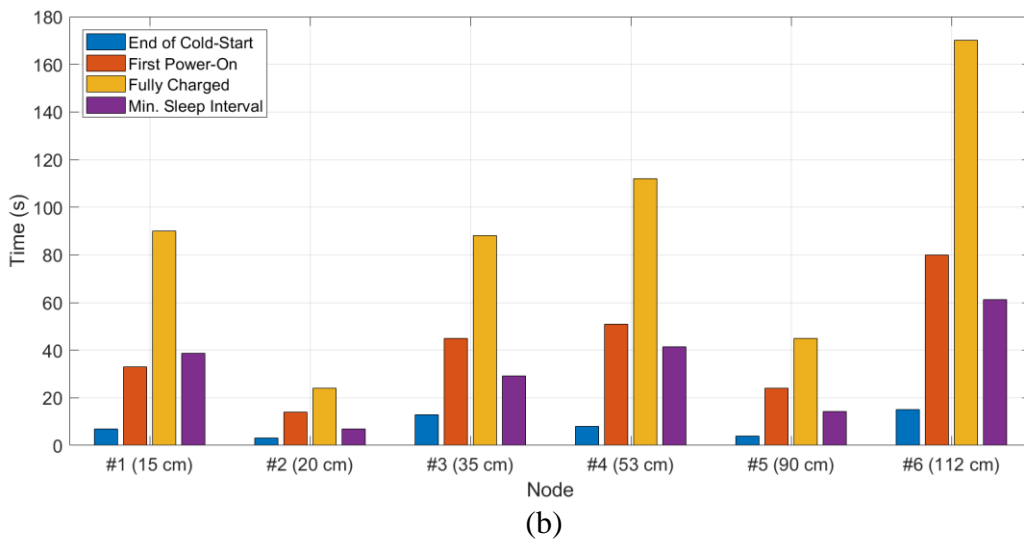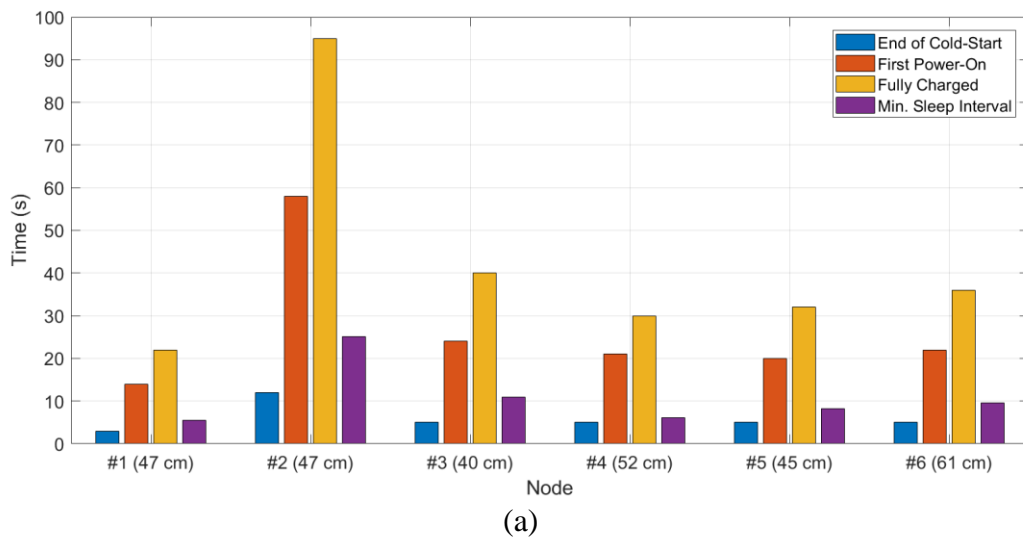

(a)

(b)

Fig. 55. Measured charging times of the six different nodes for (a) setup 1 and (b) setup 2 in the car engine compartment. [45]

It is worth noticing that the reported distances are purely indicative because they do not consider the obstacles interposed between the transmitter and the receivers, as can be evinced by charging times of nodes #1 and #2 of setup 1, sharing the same link distance.

In particular, it can be evinced that the real scenario is sensibly complex from the EM point of view and allows to increase the power budget of the most critical positions with respect to the targeted -10 dBm, thus assuring the feasibility of the proposed energizing approach, also because of the presence of the metallic shield of the hood placed over the engine compartment acting as a resonance chamber.

These results demonstrate that one illuminator with a maximum EIRP of 27 dBm is capable of transferring the energy of 4.8 mJ required to fully charge the sensor node in less than 170 seconds in the worst case of 112-cm distance between illuminator and node, under NLOS conditions.

Hence, these node charging times prove to be consistent with a monitoring system schedule of data communication every five minutes, which is perfectly reasonable for the targeted application.

Conclusion

The activities described in this thesis have been dedicated to the conception, the theoretical and numerical design of novel RF wireless systems, to be exploited within the broad paradigm of the IoT for future biomedical and industrial applications, such as indoor localization and energy-autonomous communication.

In particular, a novel and agile portable microwave radar for tridimensional tracking in indoor environments has been presented, together with a suitable realization of the associated wearable tags. The proposed system enables angular scanning of the azimuth and the elevation planes of the tag locations and exploits the RSSI-monitoring to retrieve not only the reader-tags distance, but also the tags' height thus allowing a well-approximated 3-D localization of tagged people (or objects) in indoor environments that are typically harsh from the EM point of view.

Secondly, a SIL radar for normal and deep breath monitoring has been developed and tested, with the final aim of creating a fully wearable prototype with a pocket-size receiver combined with the SILO architecture in a unique sensor, thanks to the design of a circuit for SWIPT composed of a fully passive peak detector and a voltage-doubler rectifier. This has been achieved also with experimental studies conducted

on SWIPT for FM signals coming from the most common wireless protocols, i.e., BLE.

Finally, moving on from the biomedical field to industrial applications, the bottom-up design of a self-deployable wireless RF system for remote monitoring in the automotive sector has been projected and realized. The system is based on customized RF energy sources, the illuminators, designed on purpose to be robust in EM harsh environments and able to sustain the operations of battery-less sensor nodes based on low-power communication technologies, such as LoRa. The overall system has been consistently characterized to demonstrate remote node IDs and parameters monitoring with no need for batteries on-board of the nodes. The design choices for both the illuminator and the nodes architectures have been obtained to realize wireless monitoring of complex environments, with highly efficient energy harvesting capabilities and robustness with respect to the involved environment. For any measurements carried out, the operation of the nodes has been demonstrated with charging times compatible with sensing operations.

References

[1] J. Hayter, "People who have Alzheimer," *The American Journal of Nursing*, vol. 74, no. 8, pp. 1460-1463, Aug. 1974.

[2] F. Antoniazzi, G. Paolini, L. Roffia, D. Masotti, A. Costanzo, and T. Salmon Cinotti, "A Web of Things Approach for Indoor Position Monitoring of Elderly and Impaired People," *21st Conference of Open Innovations Association (FRUCT)*, Helsinki, Finland, pp. 51-56, 2017.

[3] M. F. Mendez, J. S. Shapira, and B. L. Miller, "Stereotypical movements and frontotemporal dementia," *Movement Disorders,* vol. 20, no. 6, pp. 742-745, Mar. 2005.

[4] H. T. Cheng and W. Zhuang, "Bluetooth-enabled in-home patient monitoring system: Early detection of Alzheimer's disease," *IEEE Wireless Communications*, vol. 17, no. 1, pp. 74-79, Feb. 2010.

[5] A. Larab, R. Bastide, and B. Rigaud, "Detection of space confusion of people with Alzheimer disease," *2010 3rd International Conference on Biomedical Engineering and Informatics*, Yantai, China, pp. 1473-1476, 2010.

[6] M. Fischer, M. Renzler, and T. Ussmueller, "Development of a Smart Bed Insert for Detection of Incontinence and Occupation in Elder Care," *IEEE Access*, vol. 7, pp. 118498-118508, 2019.

[7] S. Amendola, L. Bianchi, and G. Marrocco, "Movement Detection of Human Body Segments: Passive radio-frequency identification and machine-learning technologies," *IEEE Antennas and Propagation Magazine*, vol. 57, no. 3, pp. 23-37, Jun. 2015.

[8] T. Andriamiharivolamena, A. Vena, E. Perret, P. Lemaitre-Auger, and S. Tedjini, "Chipless identification applied to human body," *2014 IEEE RFID Technology and Applications Conference (RFID-TA)*, Tampere, Finland, pp. 241-245, 2014.

[9] H. Y. Yu, J. J. Chen, and T. R. Hsiang, "Design and Implementation of a Real-Time Object Location System Based on Passive RFID Tags," *IEEE Sensors Journal*, vol. 15, no. 9, pp. 5015-5023, Sep. 2015.

[10] T. Ussmueller, D. Brenk, J. Essel, J. Heidrich, G. Fischer, and R. Weigel, "Roundtrip-Time-of-Flight based localization of passive multi-standard RFID-tags," *2012 IEEE International Conference on Wireless Information Technology and Systems (ICWITS)*, Maui, HI, USA, pp. 1-4, 2012.

[11] M. B. Akbar, D. G. Taylor, and G. D. Durgin, "Hybrid Inertial Microwave Reflectometry for mm-Scale Tracking in RFID Systems," *IEEE Transactions on Wireless Communications*, vol. 14, no. 12, pp. 6805-6814, Dec. 2015.

[12] L. Catarinucci et al., "An IoT-Aware Architecture for Smart Healthcare Systems," *IEEE Internet of Things Journal*, vol. 2, no. 6, pp. 515-526, Dec. 2015.

[13] S. R. B. Shree, H. S. Sheshadri, R. Shivakumar, and H. S. V. Kumar, "Design of embedded system for tracking and locating the patient suffering from Alzheimer's disease," *2014 IEEE International Conference on Computational Intelligence and Computing Research*, Coimbatore, India, pp. 1-5, 2014.

[14] GPS SmartSole wearable tracking solution for wandering, *Online*, Available: http://gpssmartsole.com

[15] N. Decarli, F. Guidi, and D. Dardari, "Passive UWB RFID for Tag Localization: Architectures and Design," *IEEE Sensors Journal*, vol. 16, no. 5, pp. 1385-1397, Mar. 2016.

[16] E. Borelli et al., "HABITAT: An IoT Solution for Independent Elderly," *Sensors*, vol. 19, no. 5, pp. 1258-1280, 2019.

[17] G. Paolini, D. Masotti, F. Antoniazzi, T. Salmon Cinotti, and A. Costanzo, "Fall Detection and 3-D Indoor Localization by a Custom RFID Reader Embedded in a Smart e-Health Platform," *IEEE Transactions on Microwave Theory and Techniques*, vol. 67, no. 12, pp. 5329-5339, Dec. 2019.

[18] D. Loreti et al., "Complex reactive event processing for assisted living: The Habitat project case study," *Expert Systems with Applications*, vol. 126, pp. 200-217, Jul. 2019.

[19] M. Del Prete, D. Masotti, N. Arbizzani, and A. Costanzo, "Remotely Identify and Detect by a Compact Reader With Mono-Pulse Scanning Capabilities," *IEEE Transactions on Microwave Theory and Techniques*, vol. 61, no. 1, pp. 641-650, Jan. 2013.

[20] D. Schreurs, M. Mercuri, P. J. Soh, and G. Vandenbosch, "Radar-based health monitoring," *2013 IEEE MTT-S International Microwave Workshop Series RF and Wireless Technologies for Biomedical and Healthcare Applications (IMWS-BIO)*, Singapore, pp. 1-3, 2013.

[21] L. Chioukh, H. Boutayeb, L. Li, L. Yakia, and K. Wu, "Integrated radar systems for precision monitoring of heartbeat and respiratory status," *2009 Asia Pacific Microwave Conference*, Singapore, pp. 405-408, 2009.

[22] T. S. Horng, "Self-injection-locked radar: an advance in continuous-wave technology for emerging radar systems," *2013 Asia Pacific Microwave Conference*, Seoul, South Korea, pp. 566-569, 2013.

[23] C. Li, Z. Peng, T. Y. Huang, T. Fan, F. K. Wang, T. S. Horng, J. M. Muñoz-Ferreras, R. Gómez-García, L. Ran, and J. Lin, "A Review on Recent Progress of Portable Short-Range Noncontact Microwave Radar Systems," *IEEE Transactions on Microwave Theory and Techniques*, vol. 65, no. 5, pp. 1692-1706, May 2017.

[24] F. K. Wang, C. J. Li, C. H. Hsiao, T. S. Horng, J. Lin, K. C. Peng, J. K. Jau, J. Y. Li, and C. C. Chen, "A Novel Vital-Sign Sensor Based on a Self-Injection-Locked Oscillator," *IEEE Transactions on Microwave Theory and Techniques*, vol. 58, no. 12, pp. 4112-4120, Dec. 2010.

[25] C. Hsu, L. Hwang, F. Wang, and T. Horng, "Wearable Vital Sign Sensor Using a Single-Input Multiple-Output Self-Injection-Locked

Oscillator Tag," *IEEE MTT-S International Microwave Symposium (IMS)*, Philadelphia, PA, USA, pp. 248-251, 2018.

[26] G. Paolini, M. Feliciani, D. Masotti, and A. Costanzo, "Experimental Study of a Self-Oscillating Antenna at 5.8 GHz for Breath Monitoring," *2019 IEEE-APS Topical Conference on Antennas and Propagation in Wireless Communications (APWC)*, Granada, Spain, pp. 198-200, 2019.

[27] W. J. Fleming, "New Automotive Sensors—A Review," *IEEE Sensors Journal*, vol. 8, no. 11, pp. 1900-1921, Nov. 2008.

[28] X. Yue et al., "Development of an Indoor Photovoltaic Energy Harvesting Module for Autonomous Sensors in Building Air Quality Applications," *IEEE Internet of Things Journal*, vol. 4, no. 6, pp. 2092-2103, Dec. 2017.

[29] M. Magno, D. Kneubühler, P. Mayer, and L. Benini, "Micro Kinetic Energy Harvesting for Autonomous Wearable Devices," *2018 International Symposium on Power Electronics, Electrical Drives, Automation and Motion (SPEEDAM)*, Amalfi, Italy, pp. 105-110, 2018.

[30] Y. Ma, Q. Ji, S. Chen, and G. Song, "An experimental study of ultra-low power wireless sensor-based autonomous energy harvesting system,"

Journal of Renewable and Sustainable Energy, vol. 9, no. 5, Art. no. 054702, Oct. 2017.

[31] L. Roselli et al., "WPT related applications enabling Internet of Things evolution," *2016 10th European Conference on Antennas and Propagation (EuCAP)*, Davos, Switzerland, pp. 1-2, 2016.

[32] H. Hayashi and T. Ueda, "Requirements and considerations of energy harvesting for industrial wireless transmitter," *2012 SICE Annual Conference*, Akita, Japan, pp. 1414-1415, 2012.

[33] C. Viehweger, T. Keutel, and O. Kanoun, "Energy harvesting for wireless sensor nodes in factory environments," *2014 IEEE 11th International Multi-Conference on Systems, Signals & Devices (SSD14)*, Barcelona, Spain, pp. 1-4, 2014.

[34] S. Kim et al., "Ambient RF Energy-Harvesting Technologies for Self-Sustainable Standalone Wireless Sensor Platforms," *Proceedings of the IEEE*, vol. 102, no. 11, pp. 1649-1666, Nov. 2014.

[35] A. Berger, L. B. Hörmann, C. Leitner, S. B. Oswald, P. Priller, and A. Springer, "Sustainable energy harvesting for robust wireless sensor

networks in industrial applications," *2015 IEEE Sensors Applications Symposium (SAS)*, Zadar, Croatia, pp. 1-6, 2015.

[36] T. Ruan, Z. J. Chew, and M. Zhu, "Energy-Aware Approaches for Energy Harvesting Powered Wireless Sensor Nodes," *IEEE Sensors Journal*, vol. 17, no. 7, pp. 2165-2173, Apr. 2017.

[37] K. Li, W. Ni, L. Duan, M. Abolhasan, and J. Niu, "Wireless Power Transfer and Data Collection in Wireless Sensor Networks," *IEEE Transactions on Vehicular Technology*, vol. 67, no. 3, pp. 2686-2697, Mar. 2018.

[38] R. Trevisan and A. Costanzo, "A UHF Near-Field Link for Passive Sensing in Industrial Wireless Power Transfer Systems," *IEEE Transactions on Microwave Theory and Techniques*, vol. 64, no. 5, pp. 1634-1643, May 2016.

[39] S. Dong et al., "Hybrid Mode Wireless Power Transfer for Wireless Sensor Network," *2019 IEEE Wireless Power Transfer Conference (WPTC)*, London, United Kingdom, pp. 561-564, 2019.

[40] Z. Popovic, "Far-field wireless power delivery and power management for low-power sensors," *2013 IEEE Wireless Power Transfer (WPT)*, Perugia, Italy, pp. 1-4, 2013.

[41] D. Belo, D. C. Ribeiro, P. Pinho, and N. Borges Carvalho, "A Selective, Tracking, and Power Adaptive Far-Field Wireless Power Transfer System," *IEEE Transactions on Microwave Theory and Techniques*, vol. 67, no. 9, pp. 3856-3866, Sep. 2019.

[42] K. Zannas, H. EI Matbouly, Y. Duroc, and S. Tedjini, "Antenna design for compact RFID sensors dedicated to metallic environments," *2017 22nd General Assembly and Scientific Symposium of the International Union of Radio Science (URSI GASS)*, Montreal, Canada, pp. 1-3, 2017.

[43] L. Ukkonen, L. Sydanheimo, and M. Kivikoski, "Effects of metallic plate size on the performance of microstrip patch-type tag antennas for passive RFID," *IEEE Antennas and Wireless Propagation Letters*, vol. 4, pp. 410-413, Dec. 2005.

[44] N. Shinohara, H. Goto, T. Mitani, H. Dosho, and M. Mizuno, "Experimental study on sensors in a car engine compartment driven by

microwave power transfer," *2015 9th European Conference on Antennas and Propagation (EuCAP)*, Lisbon, Portugal, pp. 1-4, 2015.

[45] G. Paolini, M. Guermandi, D. Masotti, M. Shanawani, F. Benassi, L. Benini, and A. Costanzo, "RF-Powered Low-Energy Sensor Nodes for Predictive Maintenance in Electromagnetically Harsh Industrial Environments," *Sensors*, vol. 21, no. 2, pp. 386-403, Jan. 2021.

[46] G. Paolini, M. Shanawani, A. Costanzo, F. Benassi, and D. Masotti, "RF Energy On-Demand for Automotive Applications," *IEEE MTT-S International Microwave Symposium (IMS)*, Los Angeles, CA, USA, pp. 1191-1194, 2020.

[47] C. Wan, L. Zhao, Y. Ding, and S. Xue, "A two-phase ranging algorithm for sensor localization in structural health monitoring," *Advances in Mechanical Engineering*, vol. 9, no. 1, pp. 1-8, 2017.

[48] L. Kumar, A. Tripathy, and R. M. Hegde, "Robust Multi-Source Localization Over Planar Arrays Using MUSIC-Group Delay Spectrum," *IEEE Transactions on Signal Processing*, vol. 62, no. 17, pp. 4627-4636, Sep. 2014.

[49] G. Paolini, D. Masotti, F. Antoniazzi, T. S. Cinotti, and A. Costanzo, "Anchorless Indoor Localization and Tracking in Real-Time at 2.45 GHz," *IEEE MTT-S International Microwave Symposium (IMS)*, Boston, MA, USA, pp. 286-289, 2019.

[50] M. Y. W. Chia et al., "Electronic Beam-Steering IC for Multimode and Multiband RFID," *IEEE Transactions on Microwave Theory and Techniques*, vol. 57, no. 5, pp. 1310-1319, May 2009.

[51] J. Wu et al., "Wireless indoor localization using dynamic monopulse receiver," *The 7th European Radar Conference*, Paris, France, pp. 69-72, 2010.

[52] S. Bhilegaonkar and A. Dhande, "Mono-pulse Comparator Network System with hybrid rings," *2013 19th Asia-Pacific Conference on Communications (APCC)*, Denpasar, Indonesia, pp. 556-560, 2013.

[53] Qian Dong and W. Dargie, "Evaluation of the reliability of RSSI for indoor localization," *2012 International Conference on Wireless Communications in Underground and Confined Areas*, Clermont-Ferrand, France, pp. 1-6, 2012.

[54] P. Liang and P. Krause, "Smartphone-Based Real-Time Indoor Location Tracking With 1-m Precision," *IEEE Journal of Biomedical and Health Informatics*, vol. 20, no. 3, pp. 756-762, May 2016.

[55] G. Paolini, D. Masotti, and A. Costanzo, "Wearable RFID Tag on Denim Substrate for Indoor Localization Applications," *2019 49th European Microwave Conference (EuMC)*, Paris, France, pp. 504-507, 2019.

[56] A. Costanzo, D. Masotti, N. Arbizzani, V. Rizzoli, and F. Mastri, "A microwave sensor system based on reverse modelling of the array factor," *2012 6th European Conference on Antennas and Propagation (EUCAP)*, Prague, Czech Republic, pp. 3446-3449, 2012.

[57] C. Tseng, L. Yu, J. Huang, and C. Chang, "A Wearable Self-Injection-Locked Sensor With Active Integrated Antenna and Differentiator-Based Envelope Detector for Vital-Sign Detection From Chest Wall and Wrist," *IEEE Transactions on Microwave Theory and Techniques*, vol. 66, no. 5, pp. 2511-2521, May 2018.

[58] G. Paolini, M. Feliciani, D. Masotti, and A. Costanzo, "Toward an Energy-Autonomous Wearable System for Human Breath Detection,"

2020 International Microwave Biomedical Conference (IMBioC), Toulouse, France, pp. 1-3, 2020.

[59] M. Del Prete, A. Costanzo, M. Magno, D. Masotti, and L. Benini, "Optimum Excitations for a Dual-Band Microwatt Wake-Up Radio," *IEEE Transactions on Microwave Theory and Techniques*, vol. 64, no. 12, pp. 4731-4739, Dec. 2016.

[60] G. Paolini, Y. Murillo, S. Claessens, D. Masotti, S. Pollin, A. Costanzo, and D. Schreurs, "RF Energy Harvesting from GFSK-Modulated BLE Signals," *IEEE Topical Conference on Wireless Sensors and Sensor Networks (WiSNet)*, San Diego, CA, USA, pp.1-3, 2021.

[61] C. Chen, V. Volski, L. Van der Perre, G. A. E. Vandenbosch, and S. Pollin, "Finite Large Antenna Arrays for Massive MIMO: Characterization and System Impact," *IEEE Transactions on Antennas and Propagation*, vol. 65, no. 12, pp. 6712-6720, Dec. 2017.

[62] H. Trabelsi, G. Bouzid, F. Derbel, and M. Masmoudi, "A 863–870-MHz spread-spectrum FSK transceiver design for wireless sensor," *2008 3rd International Conference on Design and Technology of Integrated Systems in Nanoscale Era*, Tozeur, Tunisia, pp. 1-5, 2008.